Universiteit Utrecht

Long-term subsidence study of the Ameland gas field: time-dependence induced by rocksalt flow

G. Marketos, D.B.T. Broerse, C.J. Spiers and R. Govers

Final Report, June 26 2015

Earth Sciences Department, Utrecht University, Netherlands

Inquiries can be directed to
r.govers@uu.nl
Department of Earth Sciences
Utrecht University
P.O. Box 80.115
3508 TC Utrecht
The Netherlands

Executive Summary

We investigate the possible contribution of rocksalt flow to time-dependent subsidence above the Ameland gas field in isolation. We conclude that rocksalt flow can potentially contribute significantly to the observed subsidence.

It appears as if rocksalt flow can explain the observed subsidence rates only partly.

There are large uncertainties in the predicted time scale and magnitude of subsidence, largely due to underlying uncertainties in material properties.

Table of Contents

1. Introduction

The Ameland gas field, which is located under an environmentally sensitive coastal area in the North of the Netherlands, has been producing since 1986. Gas production in east Ameland has stopped almost completely from 2000 onwards, but subsidence above the gas reservoir continues (Mossop et al., 2011). The reasons behind the ongoing subsidence are not understood. A number of mechanisms by which time-dependent ground deformations can arise have been proposed, and the purpose of this document is to present results of a study commissioned by NAM with the purpose of investigating one of these mechanisms in isolation. More specifically the aim of this study has been to assess whether stress-driven flow inside a rocksalt layer (the caprock to the Dutch Rotliegend reservoirs) can cause significant time-dependent subsidence on observable time scales.

This report presents and discusses results of geomechanical models of the problem. A simplified representation of a generic gas reservoir has been used to build up an understanding of how salt flow can affect subsidence. A more complex and realistic representation of the gas reservoir under the East part of Ameland Island has been used to assess what effect the stress conditions and salt material parameters can have on the magnitude of observed subsidence. The large uncertainties in rocksalt material parameters and other inputs to the geomechanical model (e.g. geometry, elastic properties distribution) represent the biggest challenge for modelers. Work presented here helps understand how results for subsidence are affected by variations in the input parameters, while a comparison with available field data is presented as an example of how geodetic data might be used to assess the relative importance of rocksalt flow on time-dependent subsidence.

As a large number of the Dutch natural gas reservoirs are overlain by thick layers of rocksalt, the increased understanding of the rocksalt-flow mechanism gained here is not only relevant to Ameland. It is hoped that this study will help guide future more detailed (and so more accurate) subsidence modeling and prediction attempts for similar rocksalt-capped gas fields. Accurate subsidence predictions for different production scenarios are essential for devising the gas extraction strategy for the Netherlands.

2. Isolating the principle drivers of salt flow

2.1. A basic mechanical model

Our initial focus is on understanding the mechanical processes involved. This is why we construct a highly simplified version of the problem: a stylized geometry and a step decrease in reservoir pressure. The Netherlands gas reservoirs are located at a depth of approximately 4 km and have a thickness on the order of 100 meters. The overlying rocksalt layer has highly variable thickness, and is typically a few hundred meters thick.

We use a Finite Element approach (Appendix A) to solve the mechanical equilibrium equations. We assume an axisymmetric geometry as shown in Figure 1. In **Model 1** we adopt a spherical reservoir with a radius of 100 m that has its center at 4000 m depth. A uniform 400 m thick rocksalt layer directly overlies the reservoir.

The left-hand boundary in Figure 1 represents the symmetry/rotation axis, as reflected also in our choice to apply free-slip boundary conditions here. The right hand side is taken at a far enough distance (r =64 km) to ensure that all displacement components are very small there. Here we allow vertical displacements only. Similarly, the bottom boundary sits very deep (z =-48 km) so that displacements are zero: here we set vertical displacements to zero. We verified that the far field boundary conditions do not affect the response of the model in our region of interest. The free surface ($z=0$) is stress free. We used convergence tests to demonstrate that the results shown here are insensitive to further refinement in spatial and temporal discretization.

We assume that the region initially is in mechanical equilibrium, i.e., that gravity body forces are equilibrated by pre-stres-

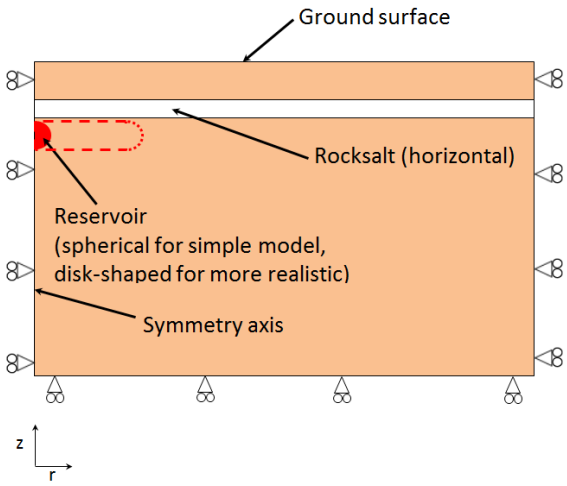

Figure 1. Schematic illustration of the domain and boundary conditions of the basic axisymmetric model that we use to identify the main drivers of surface motions. Rollers indicate that parallel displacement is possible, and perpendicular displacement is not.

ses. Here we consider perturbations to this reference state. When vertical deformation is small, this means that we can ignore gravity.

We adopt the sign convention that tension is positive. To simulate a reduction in pore pressure, we impose reduction in the mean effective stress in the model of $\Delta p = 1$ MPa throughout the spherical reservoir at time=0, i.e., $\sigma_{rr} = \sigma_{zz} = \sigma_{\theta\theta} = \Delta p$ and $\sigma_{rz} = \sigma_{r\theta} = \sigma_{z\theta} = 0$ (Appendix A). Since the model is fully linear, the 1 MPa value is not particularly relevant: the response to, e.g., a 10 MPa pressure reduction is 10x the model results. We therefore show subsidence divided by the maximum subsidence below.

Elastic properties are uniform throughout the domain of this model. The rocksalt is a linear viscoelastic (Maxwell) material. We show results at different fractions of model time and the characteristic relaxation time (Maxwell time) τ of the rocksalt (ratio of shear modulus and shear viscosity).

Marketos, Govers and Spiers recently studied a similar model ("Ground motions induced by a producing hydrocarbon reservoir that is overlain by a viscoelastic rocksalt layer: a numerical model", submitted to Geophysics Journal International in March 2015) that was based on 2D plane strain assumptions. The results of this study are very similar to the results presented here.

2.2. Time-dependent subsidence: two competing drivers

Figure 2 shows the response at $t = 0$ to the reservoir pore pressure decrease which results from (elastic) compaction of the reservoir. This appears immediately at the ground surface as subsidence. Note that there are significant horizontal surface displacements towards the source region. The subsidence is highest directly above the reservoir at the symmetry axis.

Figure 3 shows the evolution of maximum subsidence above the reservoir. At the symmetry axis, the subsidence increases rapidly to nearly 275% of the initial subsidence. The maximum subsidence occurs at approximately 45τ. Subsequently, the subsidence decreases at a slower rate.

Figure 4 shows the evolution of the subsidence bowl from the initial shape to approximately 15,000 times the characteristic relaxation time of the salt (τ). The subsidence bowl narrows and deepens from 0–8τ. From 8–18τ, the width of the bowl changes little while it deepens further. The 1149τ-curve shows that part of the subsidence has been recovered in the center. The bowl has widened beyond its initial extent and small flexural bulges with uplift have developed. Shallowing and widening

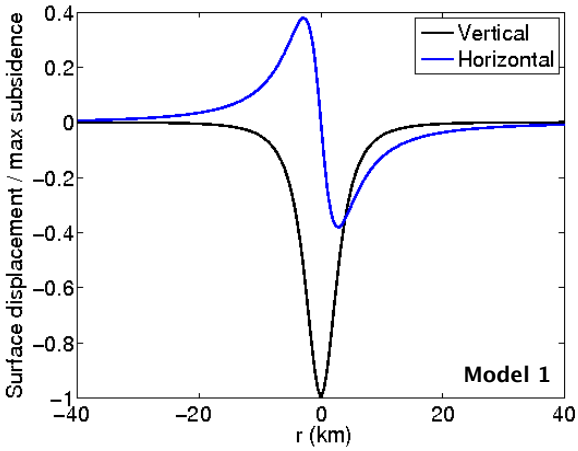

Figure 2. Immediate, elastic, surface response to a step decrease in reservoir pressure. The figure shows the normalized horizontal and vertical surface displacement versus radial distance from the centerline of the reservoir.

has continued at 14973 τ and uplift has become slightly more pronounced.

To better understand the results, we look at contours of σ_E (Figure 5), which is the maximum (or octahedral) shear stress (Appendix A). The figure also shows instantaneous velocity vectors. Initially (Figure 5a), the isotropic pressure decrease in the spherical reservoir results in a volume decrease without generating shear stresses. This is different outside the reservoir, where differences between diagonal stress tensor elements (σ_{rr}, σ_{zz} and $\sigma_{\theta\theta}$) generate shear stresses that are large near the reservoir, and decrease radially outward. The viscoelastic material flows so as to relax these shear stresses, and so viscous strain rates develop inside the rocksalt layer (see equations A.1). As can be observed in Figure 5b, the shear stresses inside the rocksalt layer relax rapidly. Note also that σ_E has started to build up inside the reservoir, and that it has also changed in the elastic layer beneath the rocksalt: this is due to the elastic stress redistribution induced by the shear stress changes inside the rocksalt layer. The overall response in the initial relaxation period is thus a result of relaxation of shear stress in the rocksalt layer. This period corresponds with the initial rapid subsidence is thus governed by **shear stress flow**.

After 3.8 Maxwell times (3.8τ) the subsidence bowl continues to deepen at a substantially slower rate. After 26.7 Maxwell times (Figure 5c) the shear stresses have relaxed almost completely. Still there is flow, albeit more slow. To understand this we need to consider the pressure (or "mean stress"), $p = \frac{1}{3}(\sigma_{rr} + \sigma_{zz} + \sigma_{\theta\theta})$ —recall that gravity and related pre-stresses are not part of this. Shear stress flow towards the reservoir has resulted in a low pressure region above the reservoir relative to the far field. This horizontal pressure gradient in the rocksalt layer drives further flow, i.e. at this stage the salt behaves like a fluid which deforms so as to equilibrate the mean stress (equivalent to the fluid pressure) inside it. This is most clearly visible in the velocity pattern, which closely resembles that of flow inside a closed conduit that is subject to a pressure gradient (i.e., Poiseuille flow). There is upwards movement of the top elastic layer as this layer gets uncoupled from the source of deformation (the reservoir), by means of the fluid-like rocksalt layer. The second period of slow subsidence recovery is thus controlled by **pressure flow**.

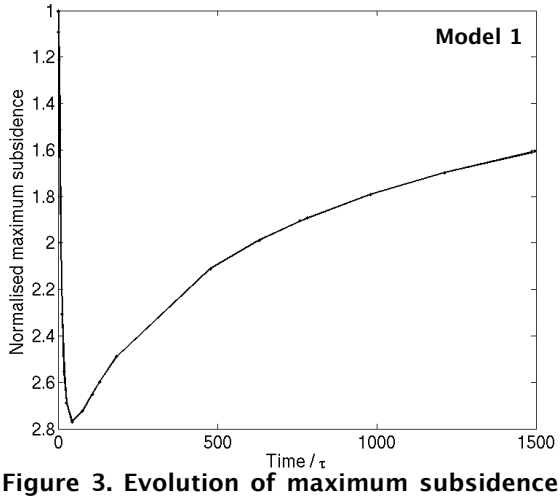

Figure 3. Evolution of maximum subsidence above the reservoir. Vertical axis: subsidence divided by initial subsidence. Horizontal axis: time since step decrease in pore pressure divided by Maxwell relaxation time.

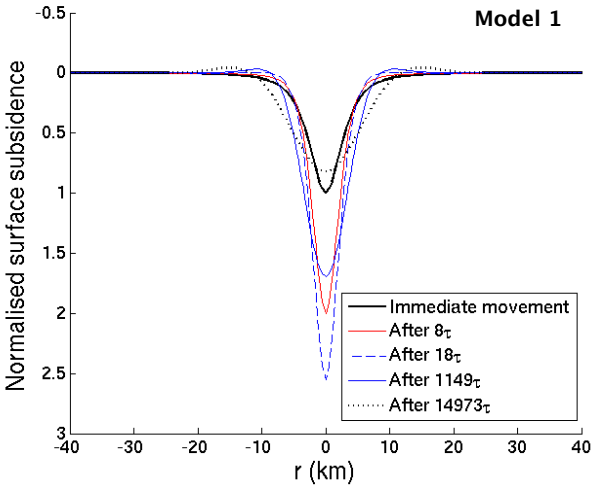

Figure 4. Evolution of the subsidence bowl. Vertical surface displacements are shown as multiples of the initial, maximum subsidence.

The conclusion from our basic mechanical model is thus that the two distinct types of subsidence response (deepening versus shallowing of the subsidence trough) can be associated with two distinct flow mechanisms: shear flow and pressure flow. These two mechanisms operate on two different timescales with the timescale for the mechanism that causes shallowing much larger than the mechanism that causes

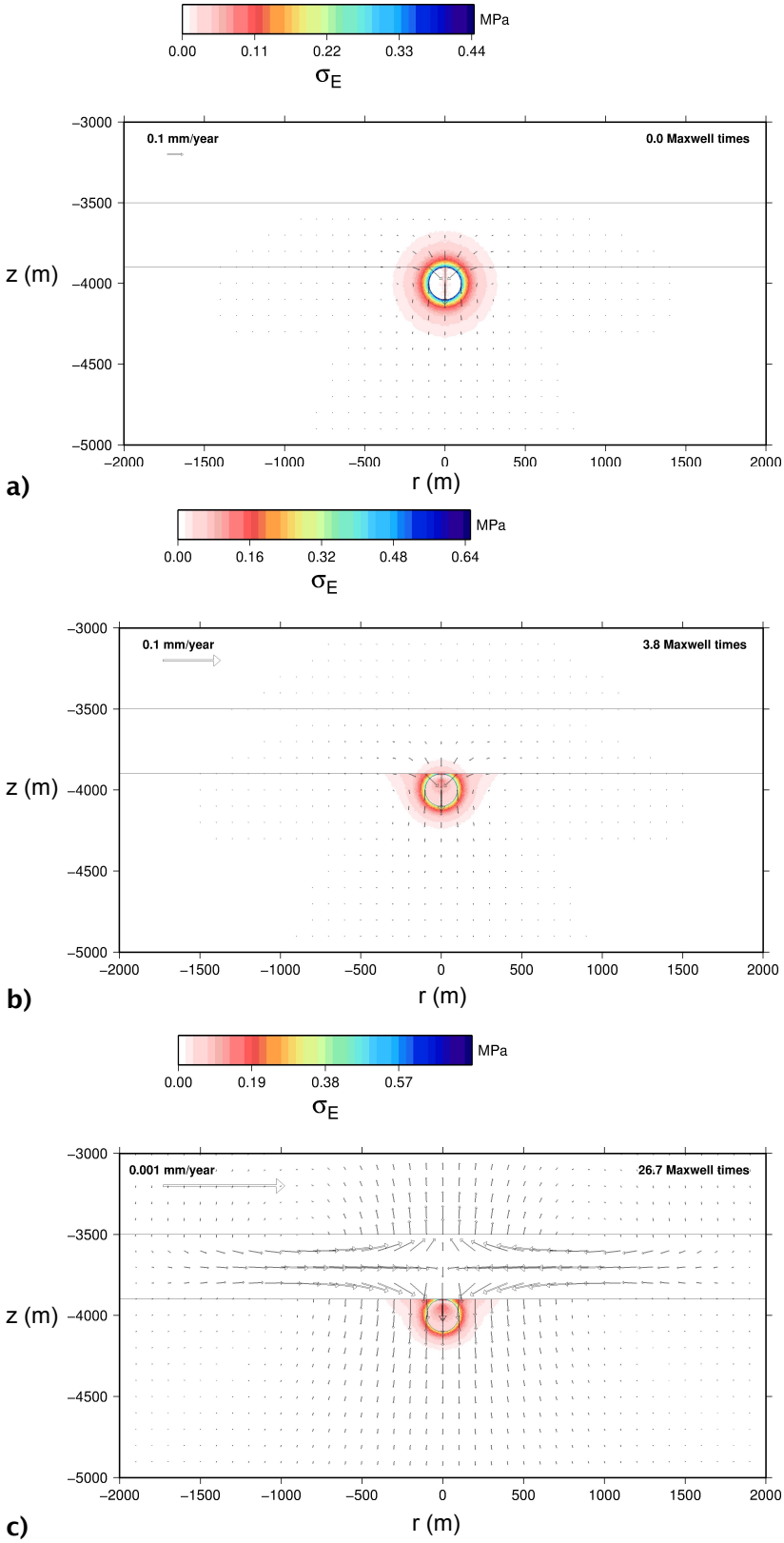

Figure 5. Maximum shear stresses and instantaneous velocities for Model 1. Notice the varying scales for both quantities. a) Directly after initial subsidence, b) after 3.8 characteristic relaxation (Maxwell) times, and c) after 26.7 Maxwell times.

deepening of the subsidence bowl.

Subsidence rate due to shear flow and uplift due to pressure flow approximately balance near the deepest point. If the efficiency of, for instance, pressure flow increases the maximum subsidence will thus be less. It is therefore relevant that we next identify geometric and material property traits that shift the balance.

2.3. Relative importance of shear and pressure flow

In this chapter, we stick with the relative simplicity of Model 1 to evaluate some of the sensitivities to variations in the model.

Model 2 is a duplicate of Model 1, except that we vary the (uniform) thickness of the rocksalt layer. In all cases the viscoelastic salt layer remains in contact with the top of the spherical model reservoir. As there is no variation in the elastic properties between the layers, the initial surface displacements $(t=0)$ are identical to Figure 2.

Figure 6 plots the evolution of the maximum subsidence (for the surface point immediately above the reservoir) with time. The subsidence of Model 1 is shown for reference. It shows that the thickness of the salt layer is very important: Essentially

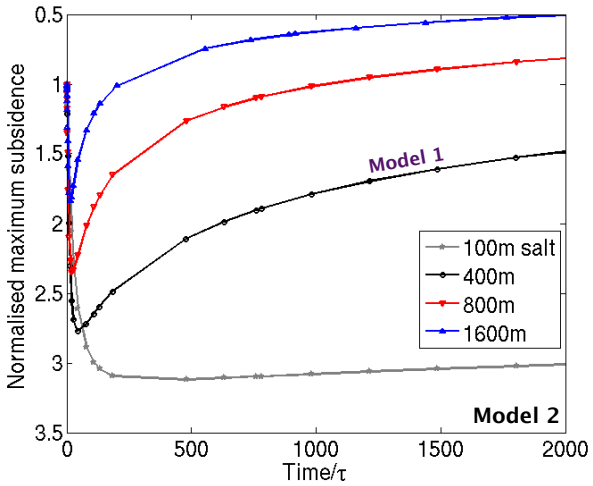

Figure 6. Sensitivity of maximum subsidence to rocksalt layer thickness. Displacements are normalized by the maximum initial subsidence value. Time is expressed as a fraction of the characteristic relaxation time of the viscoelastic material.

the thicker the salt layer is, the smaller the maximum subsidence and the shorter the time required for it to be reached, as the surface rebounds earlier.

Initially, vertical surface velocities at the symmetry axis are similar in all models indicating that shear flow is not significantly affected by the thickness of the viscoelastic layer. The width of the rocksalt channel (i.e., the proximity of its upper and lower "friction" boundaries) is very important for horizontal velocities due to pressure flow.

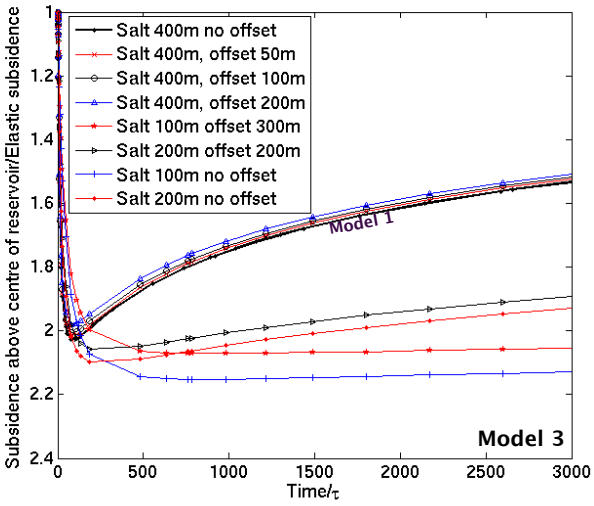

Figure 7. Sensitivity of maximum subsidence to an offset between the reservoir and the rocksalt layer. Displacements are normalized by the maximum initial subsidence value. Time is expressed as a fraction of the characteristic relaxation time of the viscoelastic material.

The width of the rocksalt layer can thus be understood as a valve on the efficiency of the pressure flow mechanism: A narrow channel suppresses pressure flow and results in prolonged subsidence by shear flow, and a wide channel in stronger pressure flow, earlier onset of recovery from subsidence and a smaller maximum subsidence.

With **Model 3** we seek to investigate the sensitivity to (mild) variation in the distance between the reservoir and the rocksalt layer. Motivation is that we observed earlier that the maximum shear stress decreases with distance from the reservoir at $t=0$ (Figure 5a). An offset thus may affect the efficiency of shear flow. Another motivation is that the Ten Boer member in the Ameland subsurface represents such a layer

that effectively is elastic on the observation time scale.

Figure 7 shows the main results. Note that these results are for 2D plane strain simulations; simulations have not been duplicated in axisymmetric conditions as all results investigated in this section have followed the same trends whether axisymmetric or plane strain (Marketos et al., submitted to GJI, 2015).

The curves for a uniform rocksalt layer thickness of 400 meters need to be compared to that of Model 1, which also has the same thickness but no offset. As is particularly visible for the model with a 200 meters offset, the maximum subsidence is less and occurs earlier. This agrees with a reduced efficiency of the shear flow mechanism. When we compare the curves for a 100 meter thick rocksalt layer, the maximum subsidence is also reduced by an offset, but the shift towards earlier time is not well constrained.

Overall, the results show that an intervening elastic layer has only a small effect on the maximum subsidence and on the time it takes for it to be attained.

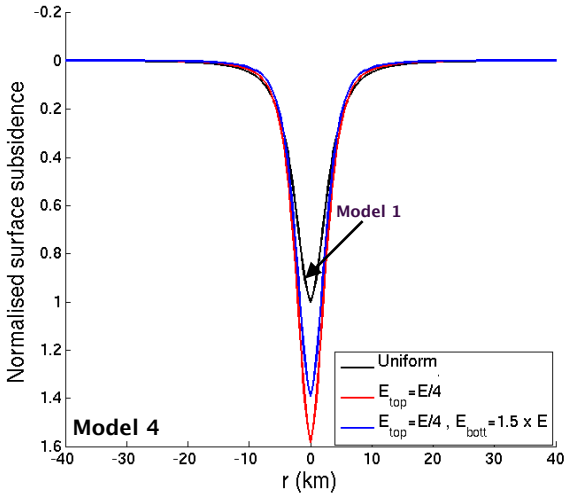

Figure 8. Sensitivity of surface subsidence to the compliance of rock layers (top=above salt, bott.=below salt). Red curve: result for a reduction of the Young's modulus to 25% of the original value. Blue curve: result for a reduction of Young's modulus to 25% in the top layer and an increase to 150% in the bottom layer. Displacements are normalized by the maximum initial subsidence of the uniform model.

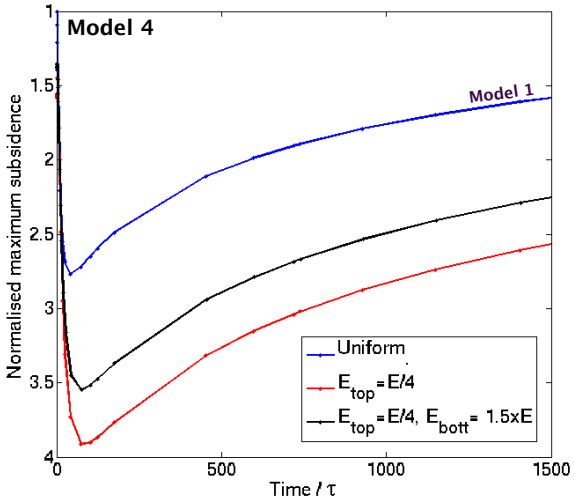

Figure 9. Sensitivity of surface subsidence to the compliance of rock layers (top=above salt, bott.=below salt). Red curve: result for a reduction of the Young's modulus to 25% of the original value. Black curve: result for a reduction of Young's modulus to 25% in the top layer and an increase to 150% in the bottom layer. Displacements are normalized by the maximum initial subsidence of the uniform model. Time is expressed as a fraction of the characteristic relaxation time of the viscoelastic material.

With **Model 4** we seek to investigate how the compliance of the surrounding rock layers affects the subsidence response. The model is again identical to Model 1, except that we make Young's modulus increase with depth. Importantly, the elasticity of the reservoir and the rocksalt layer is kept the same as in Model 1.

The red curve in Figure 8 shows that a more compliant top layer results in more surface subsidence at $t = 0$. The blue curve that a reduced compliance of the bottom layer results in less initial subsidence relative to the red curve.

The subsidence evolution for the surface point above the reservoir center is shown in Figure 9. It is important to keep in mind that the Maxwell time of the rocksalt layer is the same in models 1 and 4. The increase by a factor of 4 of the compliance (Young's modulus decreased to 25%) of the top layer results in a maximum subsidence that is about 40% higher than in the uniform case (red line). Also reducing the compliance in the bottom layer (black curve) results in approximately 25% higher maximum subsidence.

The reason for these differences is that both the top and the bottom layer affect the development of the pressure gradient in the rocksalt layer. The low pressure area above the reservoir is a consequence of mass movement by shear flow towards the reservoir. When the top layer is more compliant it flexes more easily in response to this, thereby reducing the horizontal pressure gradient in the salt layer itself. Pressure flow is therefore less effective resulting in more subsidence and a delay.

By the same token, decreasing the compliance of the lower layer results in an increase of the horizontal pressure gradient, so that the maximum subsidence is less for the black curve than for the red curve.

These findings imply the following. As the flexural rigidity of a beam depends on its thickness cubed, variations in the thickness of the top layer are thus expected to have a significant imprint on the surface response.

2.4. Apparent exponential subsidence

Mossop et al. (2011) analyzed subsidence observations in Ameland in terms of an exponential decay curve. Here we investigate what one would conclude from such an analysis 1) if indeed salt flow was the main driver of time-dependent subsidence, 2) if the observation time window was limited to the initial subsidence phase.

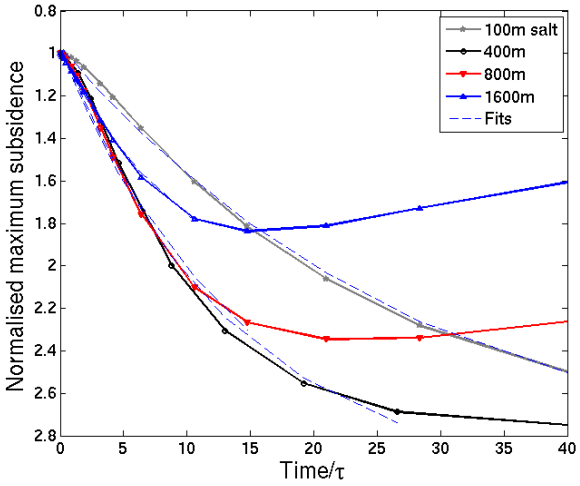

Figure 10. The initial part of the subsidence versus time curves of Figure 6. Dashed lines represent the fit of an exponential function with apparent decay time τ_{app}.

We find the best fit of our model predicted subsidence at the symmetry axis to an exponential function with apparent decay time τ_{app}. The fit is shown in Figure 10 for Models 1 and 2. Figure 11 shows the apparent decay time as function of the salt layer thickness.

Conclusions from initial subsidence data would thus strongly be influenced by the thickness of the rocksalt layer. The apparent relaxation time is a multiple of the characteristic relaxation time of the rocksalt material.

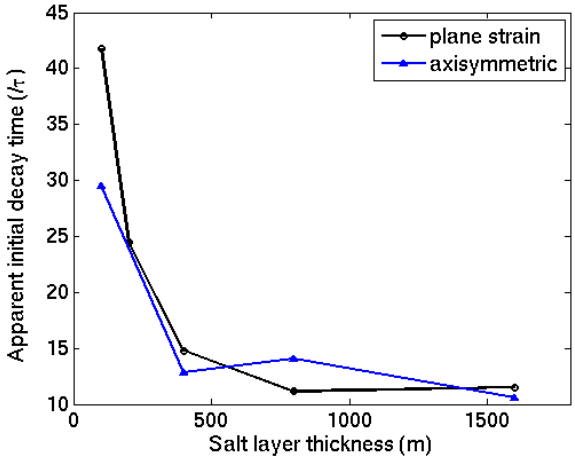

Figure 11. Apparent decay times versus salt layer thickness as obtained by the fits to the initial subsidence versus time data shown in Figure 10.

2.5. Conclusions from our basic model

Time-dependent surface subsidence is driven first by shear stress-driven flow in the rocksalt layer resulting in rapid and significant subsidence beyond the elastic response.

A second, and slower phase is driven by pressure-driven flow and results in a decrease of the subsidence.

The thickness of the rocksalt layer and the vertical layering of the elastic properties significantly affect the maximum subsidence and the moment when this occurs.

Extrapolating subsidence observations will lead to incorrect conclusions because pressure flow is not dominant initially.

3. Rocksalt rheology

3.1. Introduction

The behavior of rocksalt is complex (Spiers et al., 1990; van Keken et al., 1993; Carter et al., 1993). When subjected to a differential stress at high enough temperature, a rocksalt sample will show an initial (and not necessarily linear isotropic) elastic response. Subsequently, it will incur some small amount of permanent deformation during a transient period when the strain rate decreases with time. Eventually, substantial strain can be accumulated during steady-state creep.

Here we approximate the rheology of rocksalt by linear, isotropic elasticity and steady-state viscous flow (Appendix A), i.e., we ignore transient creep with the idea that it results in very limited amount of strain (and therefore subsidence). However, we come back to this assumption about transient creep in Section 4.4.4.

The steady-state viscosity of rocksalt strongly depends on temperature, grain size and on (small) amounts of water. It is also affected by rocksalt composition, and the presence or absence of impurities that can block or inhibit some of the micro-mechanisms that lead to flow (e.g. dislocation glide). Effective shear stress and grain size exert primary controls on which of several micro-mechanisms operate at given conditions. Possible micro-mechanisms include non-linear dislocation glide and climb, as well as diffusion creep. The micro-structure and grain size evolves during deformation. This makes the development of a unifying theory that describes steady-state rocksalt rheology at all conditions difficult.

The majority of the parameters that control the steady-state viscosity are poorly constrained for the Ameland field. Only the temperature is known relatively accurately, this is approximately 100°C (e.g., Breunese et al., 2003). Given that rocksalt is an excellent thermal conductor, the temperature gradient within the rocksalt member is expected to be small and is neglected here. The grain size is expected to be between 3 and 20 mm (NAM, 2013, Breunese et al., 2003), which is a relatively wide range. As a consequence, the linear viscosity can vary widely.

Another unknown is the natural (tectonic) stress state of the crust. Warners-Ruckstuhl et al. (2013) find a NW-SE directed strike-slip stress regime with low maximum shear stress for this region. We therefore assume that initial stresses are absent. The shear stresses applied to rocksalt due to gas extraction can be roughly estimated to be up to a maximum of a third of the pore pressure decrease magnitude (less than 50 MPa for the Ameland field, see Figure 16) if the rocksalt were in contact with the reservoir (Figure 5). However, as the Ten Boer formation intervenes between the rocksalt and the reservoir the maximum possible shear stress in rocksalt will be further reduced to a few MPa.

At low stresses the rate-controlling microprocess for rocksalt flow is pressure solution, for which the salt viscosity is grain size-dependent, or else lies in the transition between pressure solution and dislocation creep, with both mechanisms contributing roughly equally to the strain rate (see e.g. Spiers et al., 1990, Spiers and Carter, 1998, Urai and Spiers, 2007). This is the motivation behind the use of the linear flow law up to now. It should be further noted that all other modeling efforts for the North of Netherlands gas reservoirs have also used linear flow laws (e.g. Mossop et al., 2011, Orlic and Wassing, 2013).

Nevertheless as the exact conditions for the rocksalt are not known it is necessary here to investigate the effect of alternative options for the flow law on the observed behavior. First a combined linear and power law flow law is investigated. The former is linked to a pressure solution micromechanism, and the latter to a dislocation climb mechanism (see Carter et al., 1993). Viewed in terms of a dashpot analogue, these are assumed to be acting in series (equivalent to parallel concurrent transport processes), so that the total viscous strain rate is the sum of the strain rates for each mechanism. At high stresses, the power-law creep mechanism is rate-controlling and at low stresses the linear one. The other flow law that is investigated here is the one reported by Ter Heege et al. (2005). This flow law is based on the assumption that the micro-structure conti-

nually evolves to remain in the boundary between the dislocation creep and diffusion creep deformation mechanisms.

We use rheological equations (Appendix equation 1). For linear flow $(n=1)$, the steady-state viscosity is given by

(1) $$\eta = \left(2A_d\right)^{-1} d^{-m} \exp\left(\frac{Q_d}{RT}\right)$$

Here, A_d, m, and Q_d are material parameters (pre-exponential, grain size power and activation energy, respectively). d is the grain size, R is the gas constant, and T absolute temperature. Pressure-solution controlled viscosities for rocksalt grain size in the range of 3 and 20 mm at a temperature of 100°C yield viscosities between 5.10^{16} and 4.10^{19} Pa.s (Spiers et al., 1990).

For dislocation creep,

(2) $$\eta = \left(2A_{pl}\right)^{-1} \sigma_E^{1-n} \exp\left(\frac{Q_{pl}}{RT}\right)$$

Here, A_{pl}, n, and Q_{pl} are material parameters (Table 1; pre-exponential, stress power and activation energy, respectively). Maximum shear stress σ_E is defined in Appendix A for axisymmetric models.

Stress-strain rate curves for the above equations are given in Figure 12. Note that the combined linear and Carter et al. (1993) law, which assumes that both micro-mechanisms responsible for creep act at the same time and calculates the total strain rate as the sum of the strain rates that would have been calculated for the individual mechanisms in isolation would plot as a curve that asymptotically tends to the curves for the single mechanisms on their lower left side in Figure 12. We note here that we prefer the Carter equation for flow by pure dislocation creep, over the many other dislocation creep laws for salt which report a power law with an n-value of about 5 to 5.5 (see Ter Heege et al., 2005). This is because the Carter equation is based on data in which steady state was achieved in long term tests under confined conditions similar to those that apply for Ameland, whereas many other dislocation creep equations for salt were obtained unconfined/dilatant or in shorter term and/or higher temperature experiments, where steady state was not achieved. In addition, we note that the Ter Heege et al. (2005) values given in Table 1, adequately capture the effects of n-values close to 5.

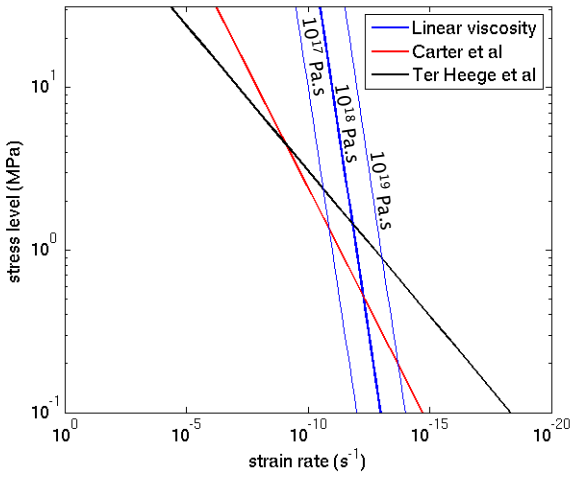

Figure 12. Steady-state viscous flow laws used in this study.

Table 1. Steady state power law viscosity parameters for equation (2)

	n	A_{pl} ($MPa^{-n}s^{-1}$)	Q_{pl} (kJ/mol)
Carter et al. (1993)	3.4±0.1	$8.1x10^{-5}$±2.7x10^{-5}	51.6±1.2
Ter Heege et al. (2005)	5.6±0.5	$10^{-1.56±0.54}$	80±6

4. Subsidence in Ameland-like axisymmetric models

4.1. Model geometry and boundary conditions

We have been provided with data of the pressures in the sandstone reservoir layers below Ameland. These are the outputs of a reservoir pore-fluid pressure analysis. Based on these data the reservoir is approximated by a disc of radius 3.75 km centered at coordinates 190000 and 610500 (Figure 13). The edges of the reservoir in the geomechanical model are curved, with a radius of curvature of 50m so as to maintain the link to the analyses discussed above, where a spherical reservoir is used.

Table 2. Elastic properties and depths of the rock units used in the simulations reported here.

Unit name	Young's modulus (GPa)	Poisson Ratio	Depth range for the unit (m)
North Sea	2	0.30	0 - 850
Chalk	10	0.25	850 - 1600
Lower Cretaceous / Triassic	16	0.25	1600 - 2000
Rocksalt (Zechstein)	30	0.35	2000 - 3250
Ten Boer	40	0.20	3250 - 3350
Rotliegendes (reservoir)	20	0.20	3350 - 3450
Carboniferous	40	0.20	3450 - 39600

NAM has provided the subsurface geometry of the Ameland field. Eight distinct layers are defined, of which two, the ROSLU_1 and the ROSLU_3 layers represent the reservoir layers. These two reservoir layers have been grouped into a single, uniform layer in our analysis as there is not enough information available to us at this point to warrant separation into two layers. Assuming that the region of interest is contained by the circle shown in Figure 13, mean positions for the surfaces that separate the layers have been calculated. These are shown in Table 2.

Material parameters used are the same to the ones used in Mossop et al. (2011) for all layers apart from the rocksalt and the reservoir. Mossop et al. (2011) state a range of elastic moduli for the Rotliegendes formation; in the next couple of models the approximate mid-range value of 20 GPa is used. Sensitivity of results to this choice will be touched upon in Section 4.5. Note that in almost all axisymmetric analyses layers are set to be horizontal and extend to the edges of the domain for the simulation, itself at a distance of 56km from the reservoir centre. This includes the Rotliegendes sandstone formation, only part of which was assigned to the reservoir. Note that as before all materials are assumed isotropic and elastic. The rocksalt (Zechstein) layer is modeled as a viscoelastic material. For this work we have treated the parameters for all layers apart from the rocksalt and the reservoir sandstone as fixed. Note that there could be relatively large uncertainties in their values too. The effect of variations in the moduli might be qualitatively rationalized using the framework developed in Chapter 2.

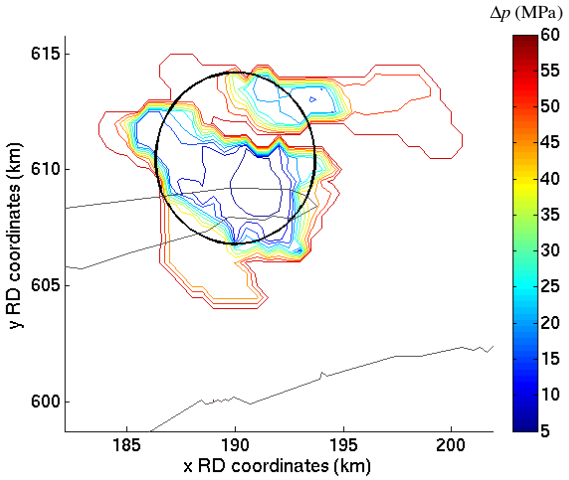

Figure 13. Contour plot of the Ameland reservoir pore pressure at a specific time instant as supplied by NAM. The circle indicates the region which has been chosen so as to determine the mean depths for each material layer in the axisymmetric model.

4.2. Response to a step decrease in reservoir pressure

The geometry of axisymmetric **Model 5** that we present here is tailored to the Ameland subsurface. For comparison with the earlier models we first investigate the response of this model to a step decrease in reservoir pressure. We assume a linear viscosity in the rocksalt, again with characteristic relaxation time τ.

Figure 14 shows the resulting surface subsidence at the symmetry axis. The subsidence is normalized by the elastic subsidence, so the result shows that rapid time-dependent subsidence maximizes at around 167% of that.

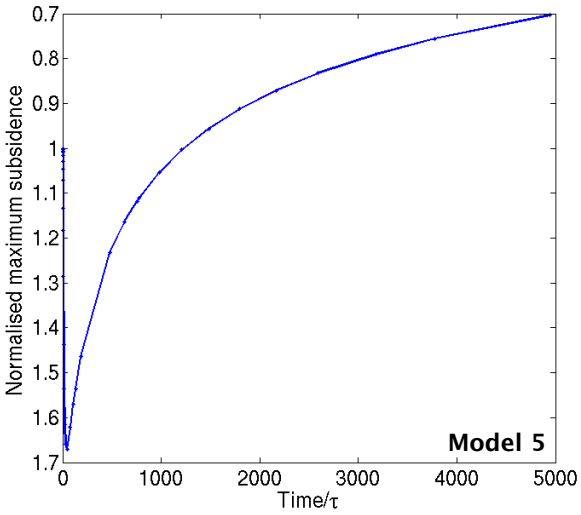

Figure 14. Evolution of maximum vertical surface subsidence for the axisymmetric Ameland simulations where a step pore pressure drop is applied.

Although different in the details, this geometrically more complex model reproduces the response of the earlier models, and supports the conclusions that have been presented earlier. For example the main conclusion is that for the Ameland reservoir too one would expect significant time-dependent displacements. Again the rate of subsidence is strongly dependent on the salt viscosity value. For what it is worth, the best fit to the initial subsidence yields an apparent decay time between 12.8 and 40 Maxwell times.

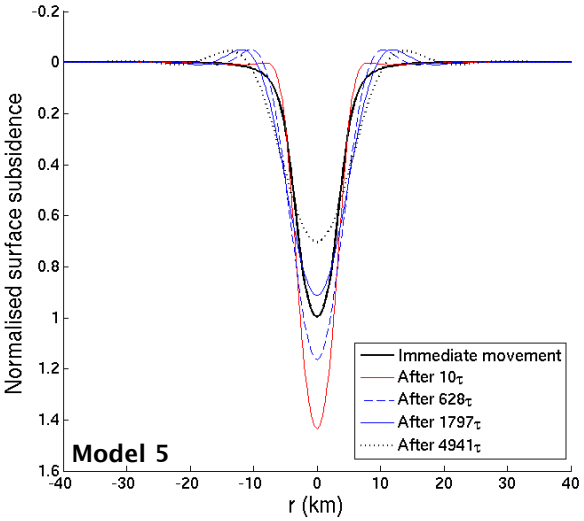

Figure 15. The subsidence bowl plotted at a number of different times after the step application of the pore pressure decrease for the Ameland simulation. Displacements are normalized by the maximum subsidence value and time by the characteristic relaxation time for the linear viscoelastic rocksalt material.

Figure 15 plots the subsidence bowl at a number of time instants after the reservoir pore pressure decrease. Again the bowl becomes initially deeper and narrower. At later stages, as before, it becomes shallower and wider, while a region of small surface uplift migrates sideways.

Overall, Model 5 shows a similar response to the geometrically more simple models.

4.3. Response to a complete pumping history

4.3.1 Model setup

The geometry of axisymmetric **Model 6** is identical to that of the previous model. Here we investigate the imprint of a realistic pumping history. Because the models are linear, the subsidence is the result of convolution of a pressure increment with the response to the step increase in pressure, i.e., delayed addition of response increments like we found for Model 5.

The reservoir pore pressure history, as provided by NAM, is the output of a Finite Difference analysis that uses pressure measurements at wells to estimate the spatial distribution of pore pressure in the Rotliegendes sandstone layers. Figure 13 is a contour plot of the data provided for a given time instant. To extract the sandstone reservoir pore pressure history as an input for our geomechanical models, we compute the minimum pore pressure in the Rotliegendes 1-12 layers at all time instants from the data. We find that this corresponds to the same spatial location, presumably a point at which pressure measurements exist. We assume a Biot pore fluid coefficient of one in our models, i.e., a pore fluid pressure change results in the same effective mean stress change on the matrix.

4.3.2 Model 6: subsidence results

The evolution of the maximum change in reservoir pore pressure is shown in Figure 16. The curve for the mean change in reservoir pore pressure displays the same trend, and we infer that using the minimum curve only has a small effect on our

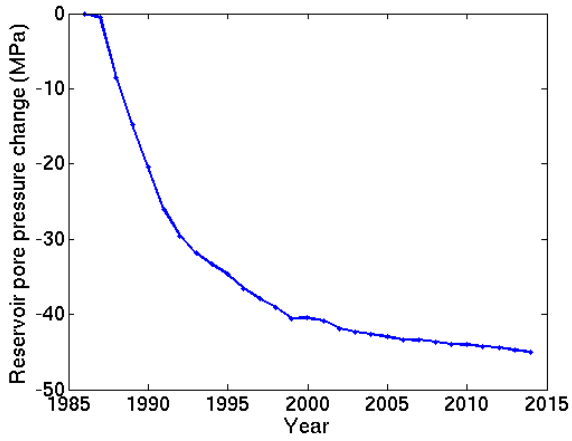

Figure 16. Maximum pore pressure change in the reservoir versus time. This is used as an input to the axisymmetric geomechanical models in this chapter.

results. In the model here, we assume a scenario where pumping stops in 2014 and reservoir pore pressure remains constant after that.

Figure 17 shows the results for Model 6. The simulation for a viscosity of 10^{17} Pa.s shows significant shear flow-driven subsidence during the first 28 years as can be seen by comparing with the "elastic salt" curve (infinite viscosity). Pressure flow and recovery from the subsidence starts even before pumping is stopped.

The simulation for a viscosity of 10^{19} Pa.s shows hardly any shear flow-driven subsidence during the first 28 years. The rock-salt Maxwell time is 28.5 years in this case and the apparent decay time, which is more than 12 times this, is longer than the pumping period. Therefore, little subsidence beyond the elastic amount occurs during this period. As is clear from the red curve, subsidence amplification occurs subsequently over a millennium period.

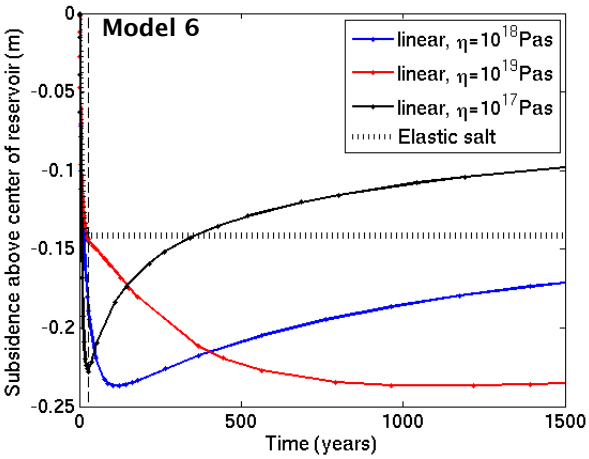

Figure 17. Evolution of maximum subsidence calculated for an axisymmetric model using the pore pressure history of the Ameland field. Results are for a linear rocksalt flow law. The dashed line represents end of pumping history, i.e., 28 years.

In the model simulation for a viscosity of 10^{18} Pa.s (Maxwell time of 2.9 years) some shear stress flow occurs during the production period but continues after that. In agreement with our understanding of the competition of the two mechanisms, shear stress flow dominates longer than for the 10^{17} Pa.s case, and so the maximum subsidence is higher. Maximum subsidence for the 10^{19} Pa.s case occurs ten times later.

We find that an (isotropic) pressure decrease results in near-perfect uni-axial vertical strain in the reservoir (in agreement with Geertsma,1973). This lends support to the fact that mechanical laboratory experiments on reservoir rocks were performed under uni-axial conditions (Mossop et al., 2011).

4.3.3 Subsidence bowl volume

The evolution of the volume of the subsidence bowl is relevant for the sediment budget and environmental imprint of the pumping. We compute subsidence bowl volume at a given moment t from

$$V_s(t) = 2\pi \int_0^\infty h(r,t) r \, \mathrm{d}r$$

where $h(r,t)$ is the vertical surface deformation of the model. Reservoir and salt layer volume changes are calculated from displacements of their boundaries using similar formulae. Figure 18a shows that V_s very closely follows the volume change of the reservoir. The volume of the subsidence does not change substantially after pumping stops, meaning that that changes in the surface deformation $h(r)$ after this (e.g., Figure 15) represent spatial redistribution only. The (small) difference between the reservoir volume change and the volume of the subsidence of the subsidence bowl is a consequence of compressibility of the elastic layers surrounding the reservoir —mostly in the stressed regions next to the reservoir lateral end.

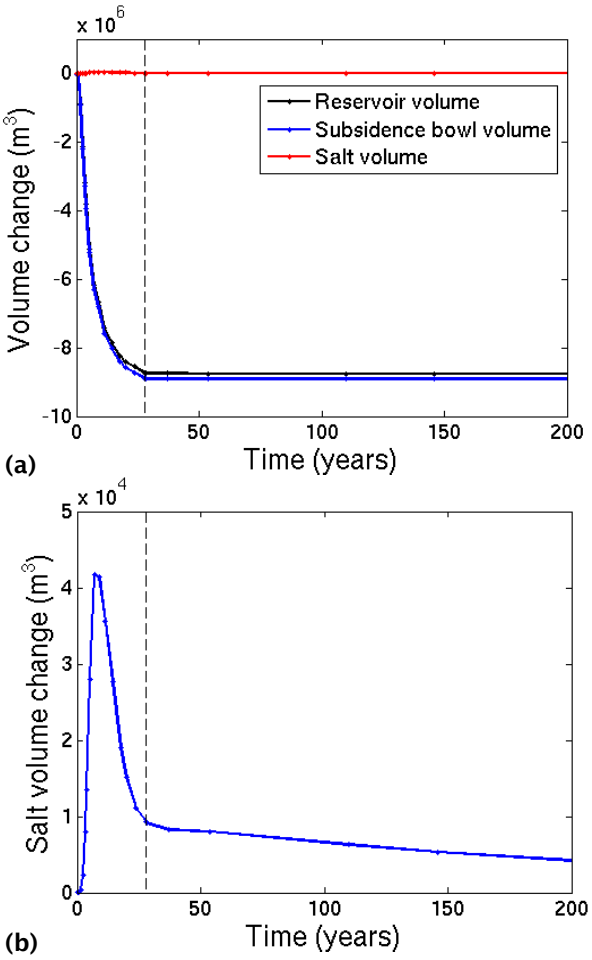

Figure 18 (a) Evolution of the volume change of the subsidence bowl, the reservoir, and the rocksalt body. The dashed line represents end of pumping history, i.e., 28 years. (b) More detailed evolution of the rocksalt body volume change.

Figures 18a and 18b demonstrate that volume changes in the salt body are relatively small. Figure 18b shows that dilation increases in the salt body during shear stress flow. Pressure flow subsequently acts to decrease this dilation again.

4.4. Surface subsidence for non-linear salt rheologies

4.4.1 Combined flow law

Model 7 is identical to Model 6, except that we use a combined flow law: linear viscous flow and power law creep based on mean parameters of Carter et al. (1993).

Figure 19 shows the evolution of the maximum subsidence. Adding power law flow to an already low viscosity of 10^{17} Pa.s has little effect on the observed subsidence; results are the same as for when only linear rocksalt creep is active. This is because the point at which the two relevant curves intersect is at a relatively high stress (just over 1MPa, see Figure 12), and so the flow of the bulk of the rocksalt, which is at a relatively low stress, will follow a linear law anyway.

For higher values of the linear viscosity the balance of the two mechanisms shifts in favor of power-law flow. For a linear viscosity of 10^{19} Pa.s there is a noticeable but small difference in maximum subsidence; this is 6% larger than with a linear flow law. This is a consequence of more shear stress flow. Also, vertical velocities are faster initially.

We conclude that using a combined linear and power law can have an effect on the subsidence evolution when the linear viscosity is relatively high. For the Carter et al. (1993) mean parameters and the specific geomechanical model for the Ameland field, this happens only for 10^{19} Pa.s.

Note also that a zoomed-in version of some of the curves in Figure 19 is shown in Figure 26. Here plots of the behavior up to 1500 years are shown so that the reader gets a fuller picture of whether the subsi-

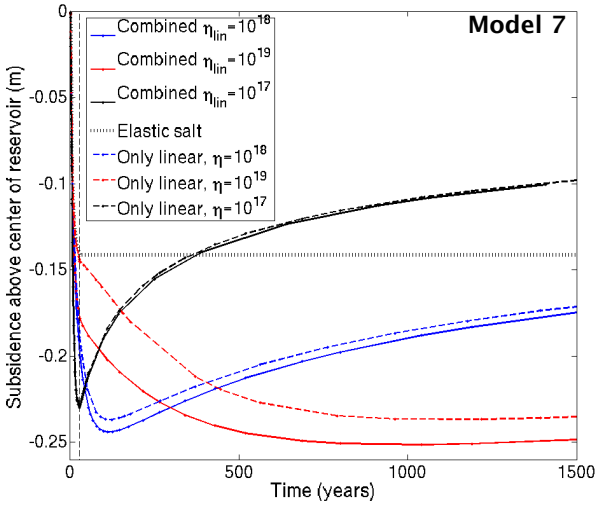

Figure 19. Evolution of maximum subsidence calculated for an axisymmetric model using the pore pressure history of the Ameland field. Results are for combined linear-power law flow. The dashed line represents end of pumping history, i.e., 28 years. The results of Model 6 (linear rheology) are shown for reference.

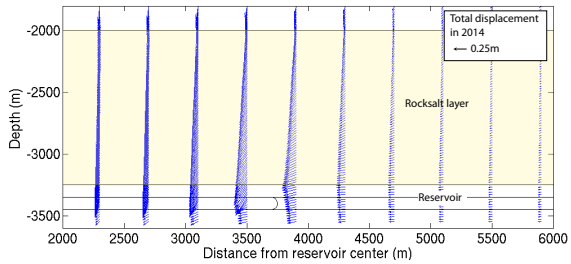

Figure 20. Model 7: Displacements within the salt layer and reservoir.

dence is expected to increase or decrease with increasing time.

Figure 20 shows displacements in the salt layer. After 28 years, vertical pipes would have become tilted by differential flow. Production engineering data may therefore be used to demonstrate salt flow if available.

4.4.2 Ter Heege flow law

Model 8 is identical to Model 6, except that we use the Ter Heege et al. (2105) flow law for the rocksalt. Figure 21 compares the subsidence evolution to the results for the combined linear and Carter et al. (1993) law for the Ameland model. For the same stress levels, the Ter Heege flow law results in higher viscosities than other flow laws if these are below approximately 1MPa (Figure 12). It therefore delays subsidence and might even lead to subsidence rates

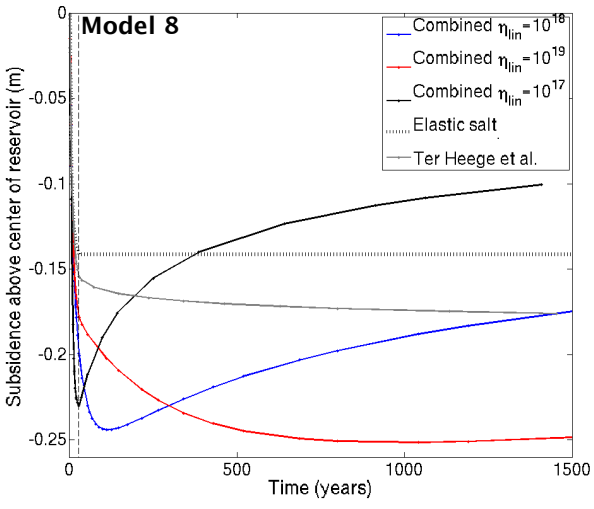

Figure 21. Evolution of maximum subsidence calculated for an axisymmetric model using the pore pressure history of the Ameland field. Results are for the Ter Heege flow law . The dashed line represents end of pumping history, i.e., 28 years. The results of Model 7 (combined rheology) are shown for reference.

becoming negligible. Uplift, and eventual decrease of subsidence, is not observed (see Figure 21). This is because the viscosities become very large and at low stresses the rocksalt is approximately elastic. In this case, pressure flow inside the rocksalt does not develop.

The Ter Heege et al. power law creep equation incorporates the effects of continuous grain size change that is thought to occur in rocksalt at strains above 5-10%. A check on the resultant deviatoric strains after approximately 30 years of salt flow has shown that these are below 0.25% everywhere. This means that based on these strain levels alone it is considered improbable that this flow law is relevant for the specific problem, as the strain levels are not high enough to ensure that the grains would have recrystallized to sizes large enough for this flow law.

Figure 22 plots the minimum linearized viscosity versus time for a number of the simulations presented above. It summarizes the behavior discussed above. The Carter et al. (1993) flow law when combined with the linear rocksalt creep law leads to effective viscosities that are lower than the linear viscosity values for rocksalt with larger grain sizes (i.e., pressure solution viscosities of 10^{18} and 10^{19} Pa.s). It therefore only produces different behavior to the linear rocksalt creep results in these situations (see Figure 19). The Ter Heege et al. (2005) creep model on the other hand

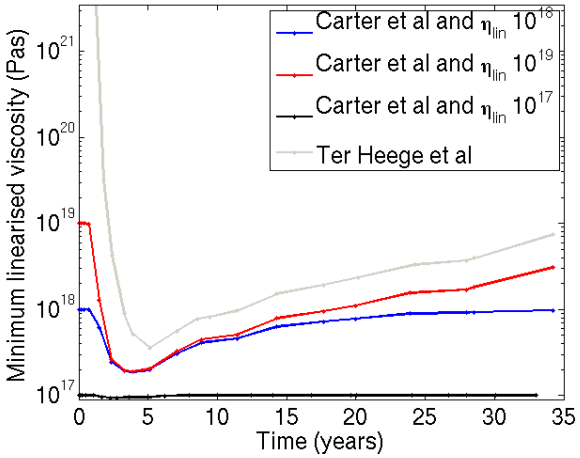

Figure 22. Evolution of minimum linearized viscosity in the simulations that use the Ameland geomechanical model with the field pressure depletion history for a number of rocksalt flow laws.

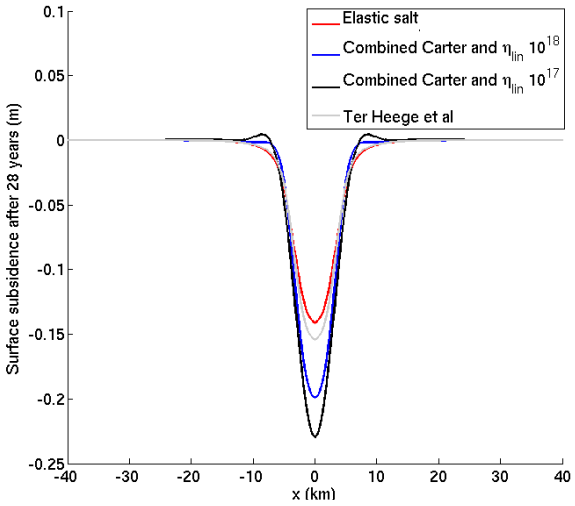

Figure 23. Subsidence bowl 28 years after production started for a number of different rocksalt flow laws. This case for axisymmetric Ameland simulations that include the pore pressure history.

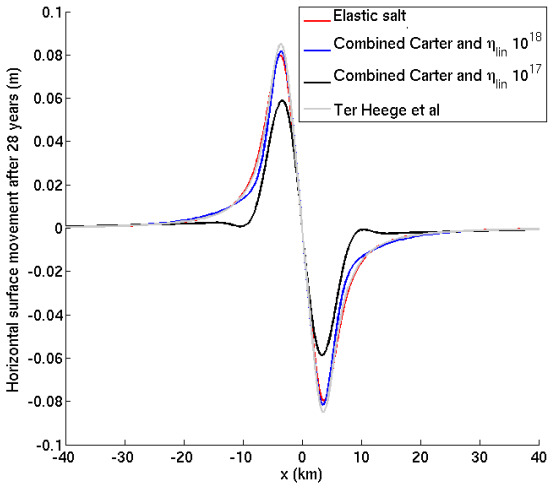

Figure 24. Horizontal surface displacements 28 years after production started for a number of different rocksalt flow laws. This case for axisymmetric Ameland simulations that include the pore pressure history.

always results in higher effective viscosities, and is not limited by any viscosity value, explaining, as discussed above, the fact that the pressure flow and recovery from subsidence does not develop.

Figure 23 shows the shape of the subsidence bowl for some key rheologies. Figure 24 shows total horizontal displacement for these same rheologies. The shape of the curves is rather insensitive to rheology. Field observations might thus not be very useful to distinguish between rocksalt rheologies.

4.4.3 Sensitivity to uncertainties in power law flow parameters

As can be observed in Table 1, there are uncertainties in the non-linear rocksalt creep parameters as result of experimental uncertainties. The effect of these variations is that the point of intersection of the two curves in Figure 12 can shift, and so lead to changes in the relative importance of the power law component in relation to the linear flow law. In **Model 9** we investigate changes in the power law input parameters that can lead to an intersection of the two model curves at different stresses. End-member linear viscosities of 10^{17} and 10^{19} Pa.s are used (Table 3). The parameter values of Table 3 have been chosen as combinations of maximum and minimum allowable values for the Carter et al. (1993) model as listed in Table 1. Only combinations that lead to curves that plot on the edges of the allowable range of curves in the

Table 3. Input parameters for Model 9.

	η (Pas)	n	A (MPa^{-n} s^{-1})	Q (kJ/mol)
Case 1	10^{17}	3.5	$10.8x10^{-5}$	50.4
Case 2	10^{19}	3.5	$10.8x10^{-5}$	50.4
Case 3	10^{19}	3.3	$10.8x10^{-5}$	50.4
Case 4	10^{19}	3.5	$5.4x10^{-5}$	52.8

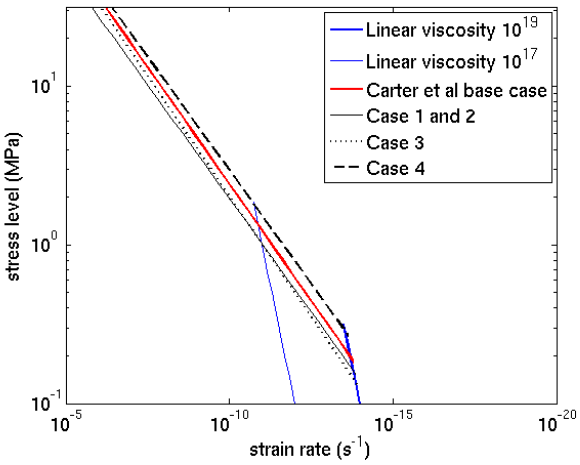

Figure 25. Rocksalt flow laws for Model 9, used to test the sensitivity of the response of the Ameland geomechanical model to uncertainties in the power law creep input parameters.

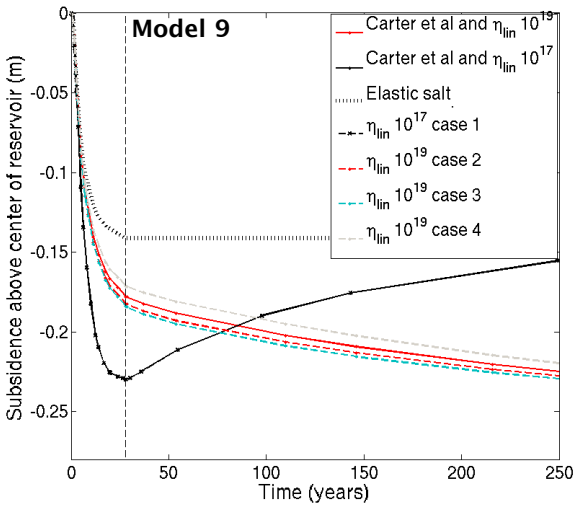

Figure 26. The evolution of maximum surface subsidence for the axisymmetric Ameland simulations that include the pore pressure history. Results for simulations that use the parameters in Tables 1 and 3.

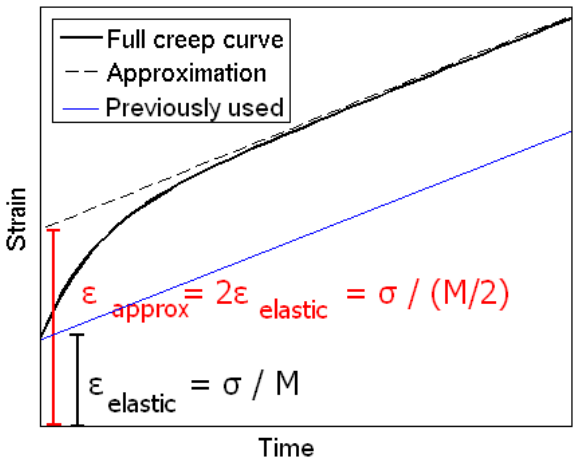

Figure 27. strain versus time plot for a material that displays transient creep, the curve used up to now in simulations, and an approximation to the transient curve. M is the relevant elastic modulus.

deformation map plot have been implemented (see Figure 25).

Figure 26 shows the resulting subsidence curves. The results for the combined linear and Carter et al. model with the mean power law parameters are also shown on this figure for comparison. The result for Case 1 is almost indistinguishable from the result for the mean input parameters. This is due to the fact that the intersection point for the two curves occurs at high stresses. This is a consequence of the low value of the linear viscosity, as discussed above, making the importance of the power law component small.

Results for the other three cases are different from the simulation for the mean Carter et al. parameters, as expected due to the high value of the linear viscosity value. Cases 2 and 3 are the ones that cause an increase in the maximum subsidence as the use of the new parameters leads to lower viscosities when the forcing is active. However this also means that the stresses relax slightly faster for these, as can be observed by the fact that the curves move closer to the one for the base case simulation for large times in Figure 26.

4.4.4 Transient creep

All the above rheologies ignore transient creep, although this may be relevant particularly in the initial stages of relaxation. Using steady-state viscous laws implies that the processes that the micro-structure is in dynamic equilibrium. However, after an increase of stress to a material element, the material microstructure takes time to readjust from its previous steady-state one to one that corresponds to the modified stress conditions. The behavior during this intermediate stage is termed transient creep and is complex to model (see e.g. Carter et al., 1993). This is because the exact form of a transient creep constitutive law depends on both the initial conditions but also the path in the three-dimensional stress for the increment applied. The simplest possible case for a stress increment is the application of a pure deviatoric stress (that is kept thereafter constant) to a sample already in equilibrium. A schematic of the expected behavior is shown in Figure 27. Note that specifically for rocksalt, a modulus that is a half to ¼ of the true elastic modulus of the material is often used (e.g. Prij, 1991) along with a power law flow equation and/or linear viscous law in order to approximate the transient creep behavior.

We implement transient rheology in **Model 10**, which is identical to Model 7 for the rest. Here a modified value of 15GPa and 7.5GPa for the salt Young's modulus is used together with a combined flow law (Table 1). Figure 28 shows that the rate of subsidence is initially slightly larger but then decreases in comparison to the simulations that use the initial modulus value. This eventual decrease in rates is due to

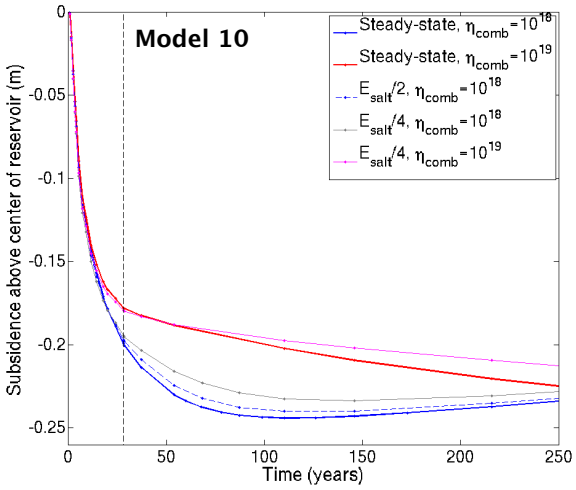

Figure 28. The evolution of maximum surface subsidence for an axisymmetric Ameland simulation that includes the pore pressure history and makes use of the transient creep approximation and linear rocksalt flow.

the fact that the rocksalt characteristic relaxation time for the transient approximation case (which controls the rate of subsidence rebound for example) is twice the one for the original simulation. The use of a lower rocksalt modulus makes little difference for the subsidence response, especially for a lower viscosity value (not shown here). The situation is however more complex; in the transient creep simulation maximum subsidence is not attained at twice the time for the initial simulation. As the exact layering of the model has now changed, the apparent decay times of the two mechanisms responsible for subsidence also have changed.

It should be noted that Model 10 also indirectly investigates the sensitivity to the rocksalt elastic modulus, the exact value of which is uncertain. The rocksalt modulus will strongly depend on its composition; here the rocksalt is assumed to be halite (Mossop et al., 2011). Note that for different salt layer compositions Breunese et al. (1993) use markedly different Young's modulus values that range from 5.5 to 30 GPa. The creep model parameters for different salt compositions will then also be different to the ones used here. The effect of the presence of salts of perhaps different compositions above the Ameland gas field is beyond the scope of the current study.

4.5. Sensitivity to reservoir elasticity parameters

Another major uncertainty in the Ameland subsidence prediction model are the elasticity parameters of the reservoir sandstone. Mossop et al. (2011) discuss sandstone modulus variability, as observed in laboratory tests on Rotliegendes sandstone samples. They also quote a range of Young's modulus values for the reservoir sandstone layer material (8.7 to 36 GPa). All simulations up to now have used a value of 20 GPa for the Rotliegendes formation Young's modulus. This section presents results of **Model 11** with a reservoir material Young's modulus of 15 and 10 GPa, values also within the range quoted by Mossop et al. (2011). We use a combined rocksalt flow law with linear viscosity 10^{18} Pa.s (Table 1).

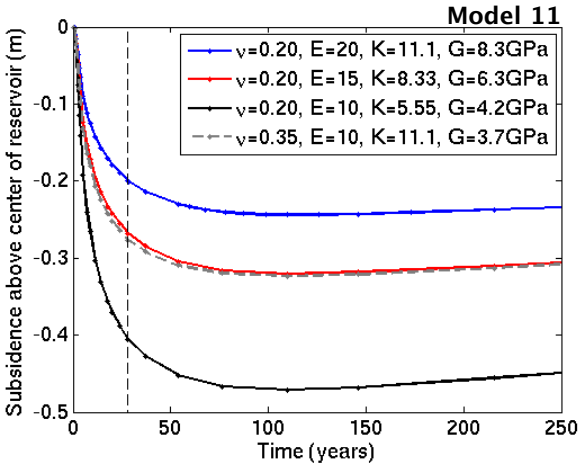

Figure 29. The evolution of surface subsidence at the symmetry axis of an axisymmetric Ameland simulation that includes the pore pressure history for linear rocksalt flow and alternate reservoir compressibilities.

The surface evolution is shown in Figure 29. The reference result (with a Young's modulus of 20 GPa) is also shown for comparison. Note that the reservoir material compressibility has a very important effect on the magnitude of subsidence. The higher it is, the larger the compressive strains at the reservoir level due to the pore pressure depletion. Hence the larger the 'volume lost' at the reservoir layer, the larger the displacements are that get registered at the surface as subsidence. Model 11 therefore highlights the importance of the rocksalt compressibility (or modulus) value as one of the factors that controls the

magnitude of subsidence, and helps motivate the conduction of more laboratory tests on the reservoir material. There also is a significant effect of Poisson ratio, which therefore also needs to be constrained further experimentally.

Note that as reservoir pore-fluid pressure is depleted, inelastic processes are also present inside the reservoir layer and a change of the resultant modulus is expected versus time. This effect has been neglected here, and so has been reservoir material creep. This has been done on purpose as the aim of this project is to investigate the effect of the rocksalt creep behavior in isolation. Apart from the above mentioned complications there is also the inherent spatial variability inside the rocksalt material that comes about from spatial differences in porosity (and other rock physical properties) due to a variable depositional environment for example.

5. Subsidence in non-axisymmetric models for Ameland

5.1. 2D variations in salt layer thickness

We find that the thickness of the salt layer exerts a critical control on the relative importance of shear flow and pressure flow, and therefore on the surface subsidence. It is therefore likely that lateral variations in this thickness are relevant. **Model 12** uses a 2D plane strain approximation to identify whether having a spatially variable salt thickness significantly affects the observed subsidence response.

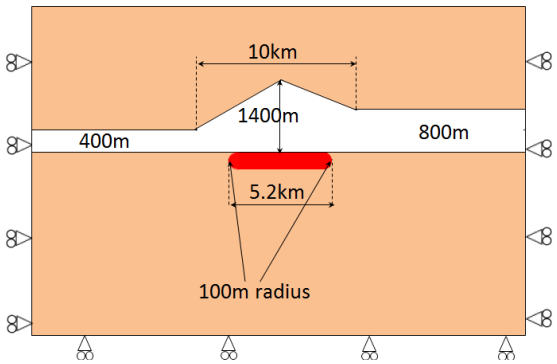

Figure 30. A sketch of the geometry for plane strain Model 12 that includes an asymmetric rocksalt layer (not to scale)

The geometry of the model is shown in Figure 30. The viscoelastic material is dome-shaped and is thicker on one side of the reservoir in comparison to the other, and the reservoir extends laterally by 5.2 km. Elastic moduli are uniform throughout the model and a 1MPa step decrease in pore pressure is applied.

As the elastic properties of all materials are the same, the subsidence immediately after the pressure drop application is symmetric about the vertical line through the reservoir center (Figure 31). However, as time progresses the surface subsidence becomes asymmetric and the deepest point of the subsidence bowl moves to the right, i.e. towards the side of the thickest salt (Figures 31 and 32). This is a significant result that merits further investigation.

Assuming that the spatial variation of the rocksalt layer thickness is well-constrained from seismic, and that rocksalt material properties are relatively uniform, results from simulations that include such asymmetries can be used to test the hypothesis of salt flow causing significant time-dependent deformations. This is because it is thought that the signal caused by salt creep flow in this case will have distinct characteristics to other major possible causes of time-dependent subsidence such as

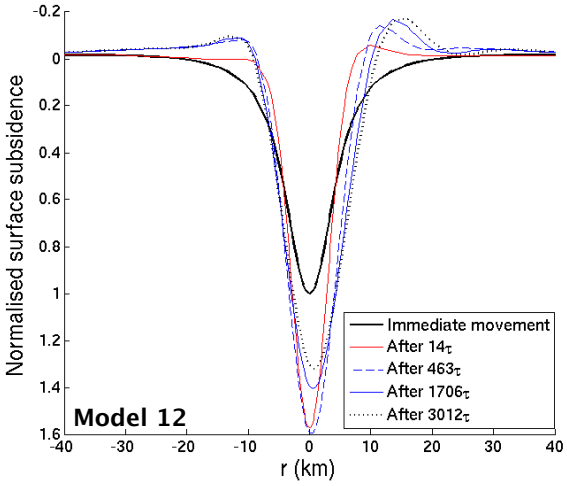

Figure 31. Subsidence bowl evolution after a step decrease in pore pressure. Vertical displacements are normalized by the maximum subsidence elastic value. Time is normalized by the Maxwell time for the linear viscoelastic rocksalt material.

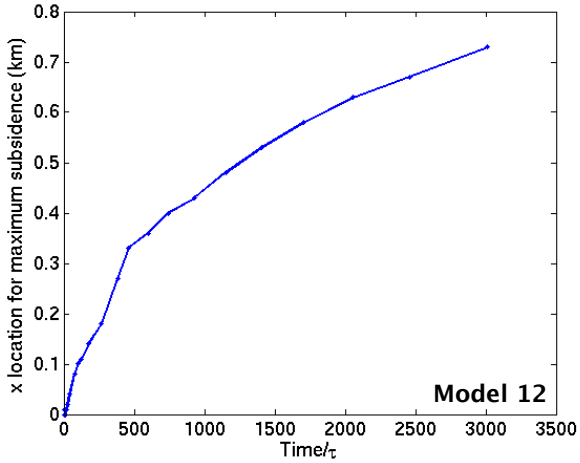

Figure 32. Evolution of the horizontal distance of the deepest point of the subsidence bowl from the center of the reservoir.

reservoir material creep, itself probably leading to more a symmetric response.

Furthermore, it could be that different salt flow laws or different viscosity values yield different time responses. It might be therefore possible to use such data to inform the choice of salt flow law or viscosity value. Finally it should be noted that the subsidence data (see Mossop et al., 2011 and Section 5.2 below) do not show any significant measurable movement of the deepest point of the subsidence bowl. However it remains to be seen whether more densely-sampled subsidence data from methods other than leveling can reveal hidden trends.

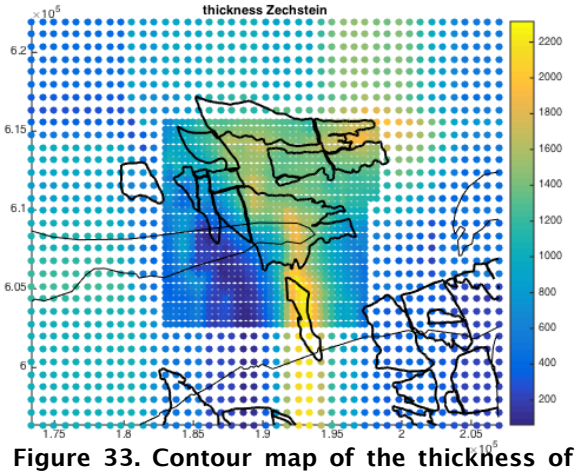

Figure 33. Contour map of the thickness of the rocksalt layer (m). Thin lines show coast lines of east Ameland and Friesland for reference. Thick lines: known gas plays (nlog.nl).

5.2. 3D model

The primary reason why 3D simulations are needed follows from our conclusion in chapter 2 that thicknesses of the rocksalt layer and the layers above it strongly affect time-dependent surface subsidence. Figure 33 shows substantial variations in the thickness of the rocksalt layer.

An additional reason is that the Ameland field is not a single field but a collection of linked sub-fields some of which have entered production after the central part of the field (Figure 13; Marquenie and Doornhof, 2005; Crouch et al., 1996). These aspects also motivate further investigation with a 3D geomechanical model.

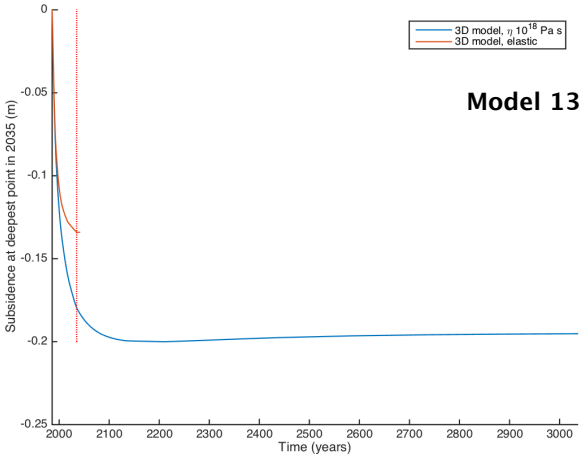

Figure 34. Maximum subsidence with time The model shows limited pressure flow in the model time interval.

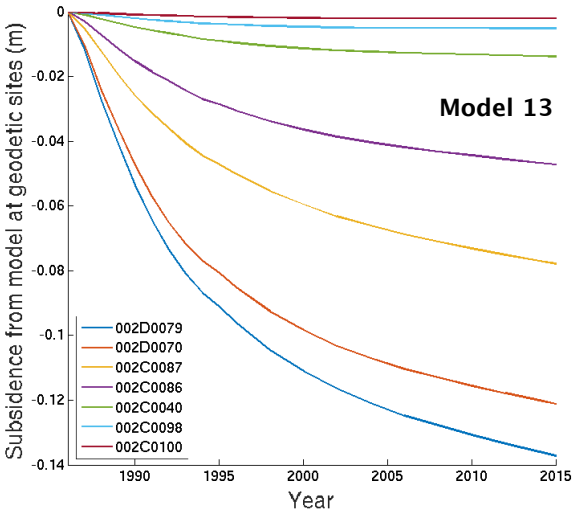

Figure 35. Model subsidence with time at observation benchmark locations.

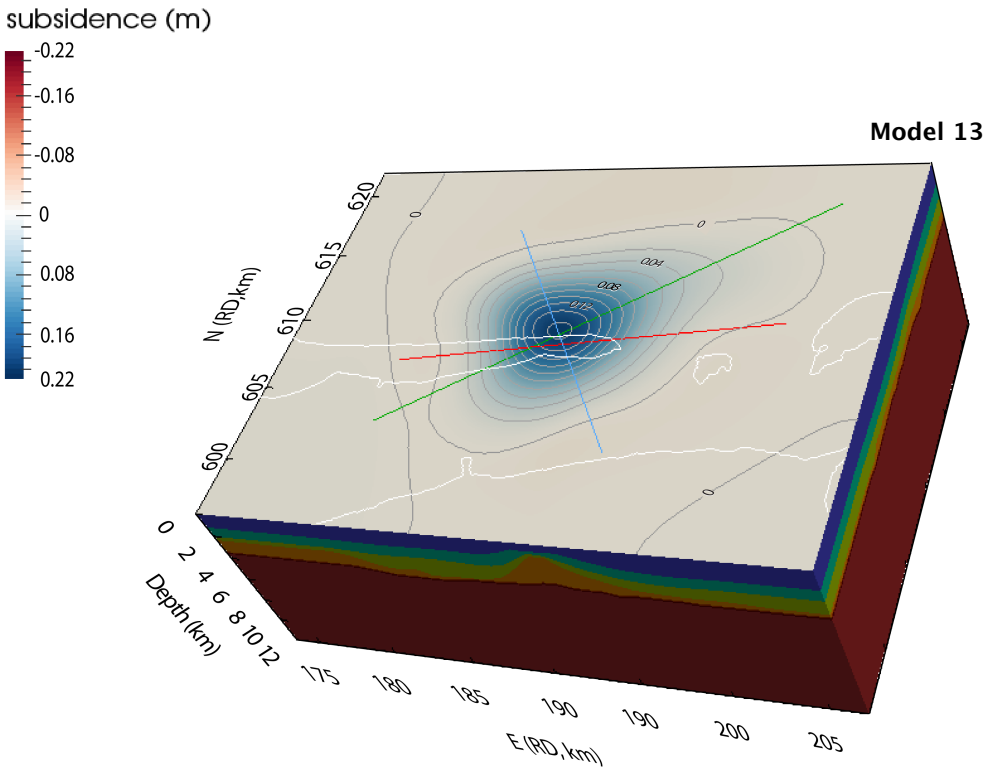

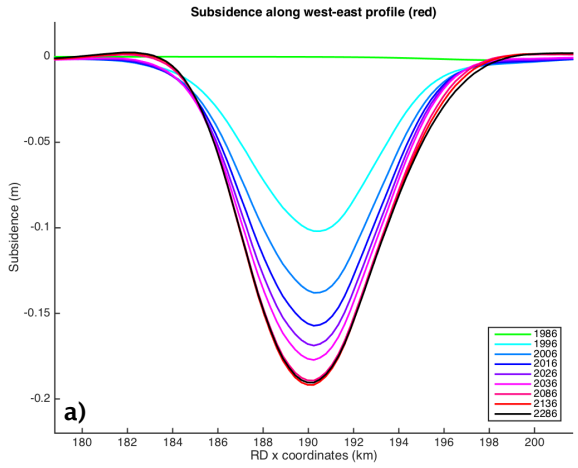

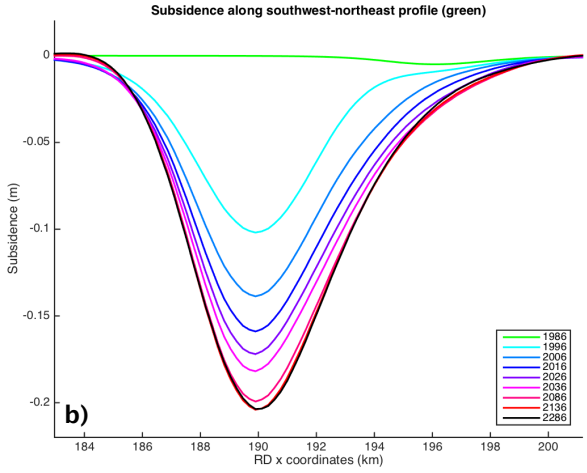

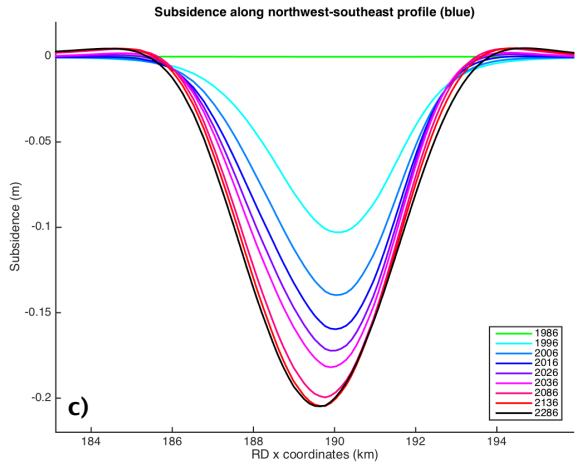

Figure 36. Surface subsidence. 3D perspective block diagrams show the subsidence bowl after 150 years of model evolution. White lines indicate the coast of east Ameland and Friesland. Profile lines of a), b) and c) are indicated. Profile subsidence lines in years 1986–2286.

The geometry of **Model 13** is based on the geometries provided by NAM, with a few minor adaptions (see box). The model contains eight layers of which the bottom layer is extended to 12 km depth. The model's coordinates are given in RD-coordinates in meters, where its dimensions are 33,600 x 25,600 x 12,000 meters, in easting (x), northing (y) and depth directions, respectively. The Rotliegendes reservoir layers have been merged into one layer to prevent very thin layers. We adopt the scenario of future pumping as given to us by NAM. Note that differs slightly from the scenario in the axisymmetric models.

Material properties are identical to those in Model 6, see Table 2. The rocksalt layer (Zechstein) creep model is linear with a viscosity of 10^{18} Pa.s.

The results in Figures 34 and 35 show the maximum subsidence evolution. Figure 36 shows the shape of the subsidence bowl after 150 years and the evolution along different profiles. One can clearly see that the subsidence is not completely symmetric, the northern part of the surface above the region subsides more than the southern parts (seen from location of peak subsidence). One cause is that salt thickness increases from the southwest (approximately 200m at the SW corner of Ameland Oost) to northeast (approximately 1400m above Westgat) with a 2000 m dome on top of easterly Ameland Oost; the other cause is that production started also in Westgat, to the northeast of Ameland. We thus confirm the anticipated imprint of 3D structure and pumping.

Box: **Modified geometry for full 3D model**. Relative to the original NAM model, a few changes have been made to the Zechstein and Ten Boer layers at the boundary of the model, to prevent very thin (2m) layer thicknesses. The Ten Boer layer has been set to a uniform 200 m thickness, which was the case in the original NAM geometry. The top of the Zechstein layer has been raised in the northwest and southeast corner to remove thin regions (that were a result of extrapolating layer interfaces towards the model edges) and ensure a thickness of at least 200 meters. This is done by setting the top of the Zechstein to a uniform depth of -2863.27 m in the area between these ranges:

- 173 km < x < 179.8 km and 615 km< y < 622 km and the points representing the top of the Zechstein to -3220 m in the area between: 202.5 km < x < 208 km and 605.5 km < y < 611.6 km

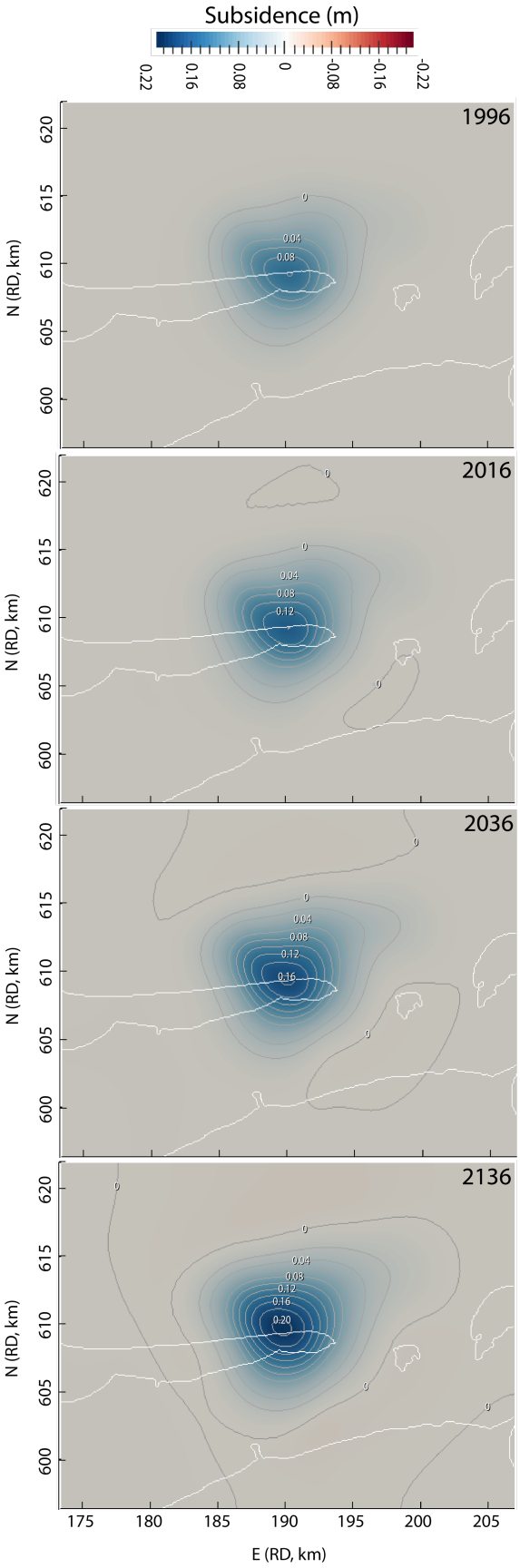

Figure 37. Model 13: Evolution of the subsidence bowl.

Similar to the axisymmetric models, we find that (isotropic) pressure decrease in the reservoir results in near-perfect uni-axial vertical strain in the reservoir.

Figure 37 shows the subsidence bowl in a geographic frame. With time, the subsidence bowl shift slightly towards the NE.

6. Comparison of model predictions and data

6.1. Ameland geodetic data

NAM has provided us with the raw data of ground surface displacements that have been collected using three different methods, leveling, INSAR and GPS. Of these leveling data is the most straight-forward to use. It is also the most extensive in time as it contains subsidence measurements throughout the entire life of the Ameland gas field. Houtenbos (2011) discusses the accuracy of these measurements.

Unfortunately only vertical displacements are available to us at the moment, except one continuous GPS station at the production location on Ameland Island with 3D displacements. Other datasets available will not used in our preliminary comparison.

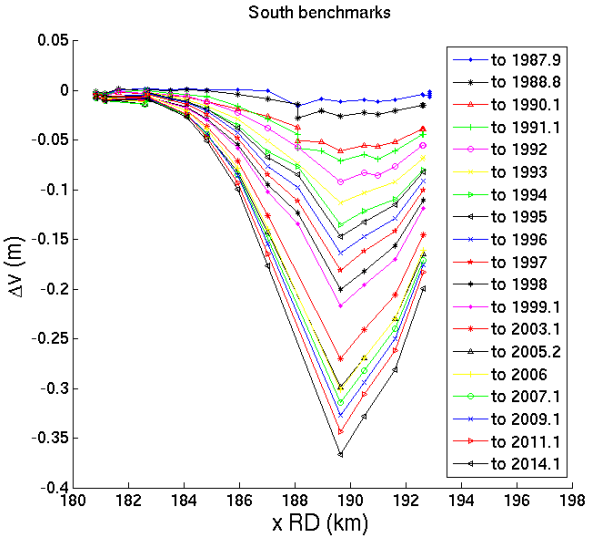

Figure 38. Evolution of the subsidence trough along a west-east line from leveling observations.

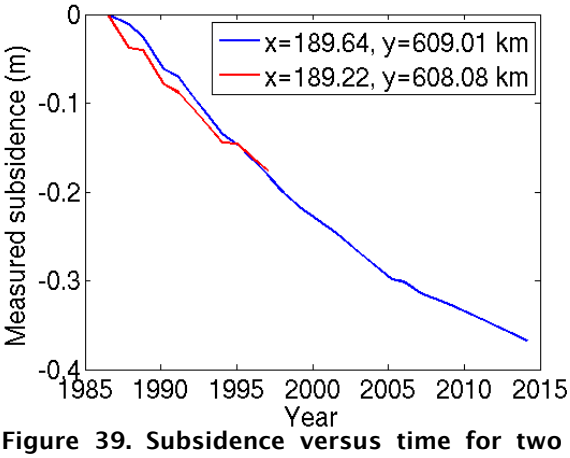

Figure 39. Subsidence versus time for two leveling benchmarks located close to the middle of the Ameland field.

The leveling benchmarks are located on an approximate east to west line on Ameland Island. Figure 38 plots the subsidence bowl as calculated from the leveling data at a number of different times. The data have been differenced from the initial leveling campaign that was conducted in 1986 on the south side of the island, while the plotting procedure neglects the small differences in the northing coordinate of the leveling benchmarks. Note that there is the underlying assumption that the point furthest away from the reservoir centre (i.e. at an x of approximately 181km) is stable. Nevertheless, the overall trends are clearly observable. There is a deepening of the subsidence bowl as time progresses.

There could also be a slight eastwards movement of the deepest point of the subsidence bowl; this point is however not clear due to the sparsity of data. Figure 39 plots the subsidence of two points close to the middle of the field where the largest values of subsidence have been observed. Measurements at one of the points show an offset after 1997: these are not included here. Even though the pressure depletion occurs at ever decreasing rates, subsidence continues with an almost constant rate. Its rate only seems to decrease slightly after 2005 to approximately 7-8 mm/year.

Figure 40 plots the time series for the continuous GPS station that is located at the Ameland Island production location. As can be seen in Figure 40(a), similar to Figure 38, there is a clear trend of increasing subsidence with time. A best fit line through the data gives a subsidence rate of 6.7

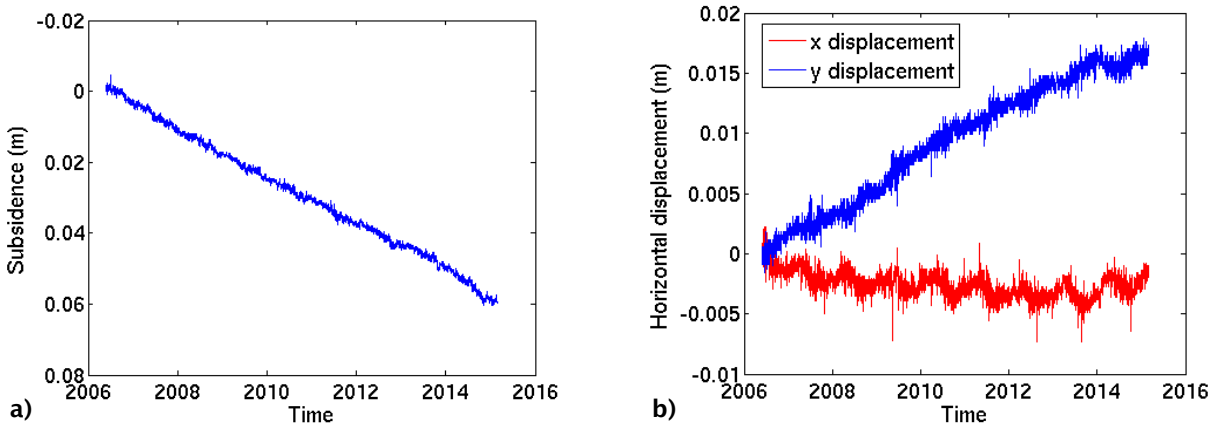

Figure 40. Continuous GPS displacement with time at the Ameland production location (a) Subsidence (b) Horizontal displacements (red line in easting direction, blue line in northing direction).

mm/year. There are however parts of the curve that show minor variations from this line. For example if the data after the middle of 2013 are used the best-fit subsidence rate is 8.8 mm/year, and even though it might be tempting to extrapolate to larger times it is not possible to do so given the data available. For example there are other timespans too for which the subsidence rate seems to be slightly increased (e.g. between the third quarter of 2006 and the middle of 2008 at 7.5mm/year) with the subsidence rate falling back to lower values. This variation indicates that in order to use GPS data a full study on errors and the causes of noise in the data needs to be conducted; at the moment it is not clear if the above mentioned differences in rates are real. What is surprising nevertheless is that between 2006 and 2014 the pressure decrease in the Ameland Oost reservoir was 1.6 MPa, a relatively low value in comparison to the total pressure decrease of over 40 MPa over the lifetime of the reservoir (see Figure 16).

Figure 40(b) shows that there might be a trend in the horizontal data in the northing direction; more analyses are required to investigate whether this is a true signal or an artifact, and whether this trend can be explained by the three-dimensional geological structure of the Ameland field. Furthermore a fuller analysis of horizontal displacements is necessary, for example it is beyond the scope of this study to compare the horizontal displacements to base horizontal displacement rates that are expected due to tectonic plates' movement, or to investigate whether the mounting of the GPS instrument can affect the signals it measures.

6.2. Preliminary comparison of models and observations

The plots above are the ones to which the results of the geomechanical analyses need to be compared to. Here however only a preliminary/qualitative comparison is attempted as no effort has been made to calibrate the geomechanical model in order to reduce the uncertainties present in it. For example the subsidence observed in the field is larger than what is predicted using the elastic parameters of Table 1. Model 11 shows that a reduction of the Young's modulus while keeping Poisson ratio the same (while still being within the range of values quoted by Mossop et al., 2011) would allow us to obtain a better match to the current maximum subsidence. However, the models presented in this report cannot fully explain the observed surface subsidence.

Figure 41 suggests that a linear viscosity value of 10^{17} Pa.s is not a plausible candidate for the rocksalt as it seems to lead to decreased subsidence rates, something that is not supported by the field data.

Model results show that a decrease in subsidence rate should be expected (Figure 41). There are not enough field data points yet so as to allow for a clear conclusion to

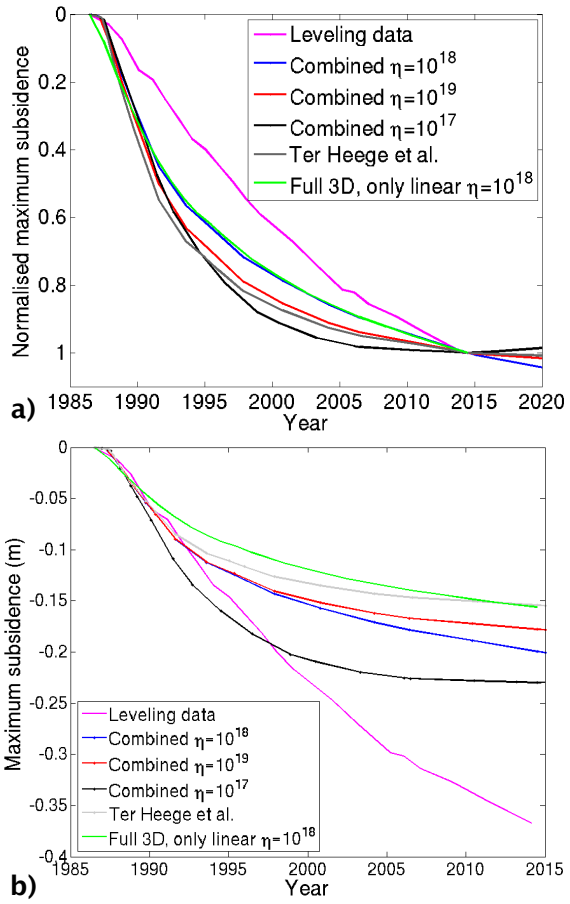

Figure 41. Comparison of model predicted maximum subsidence with leveling data. a) Normalized by maximum subsidence in 2014, b) maximum subsidence.

be made, but it seems that there is a smaller-than-expected subsidence rate decrease in the field. This means that apart from the rocksalt flow mechanism there might be another mechanism that acts in parallel to rocksalt flow and causes additional subsidence. A good candidate might be reservoir sandstone creep or stress-level dependent compliance.

Qualitatively the observed shape of the subsidence bowl looks similar to the one expected on the basis of the Finite Element simulation results, but it is more narrow (Figure 42).

Figure 35 plots the 3D model predictions for the evolution of rocksalt-induced subsidence at a number of benchmark locations. The shapes of these curves do not vary much from the one for maximum subsidence (Figure 34) indicating that uncertainties over the location of the deepest point of the field subsidence bowl do not affect our conclusions.

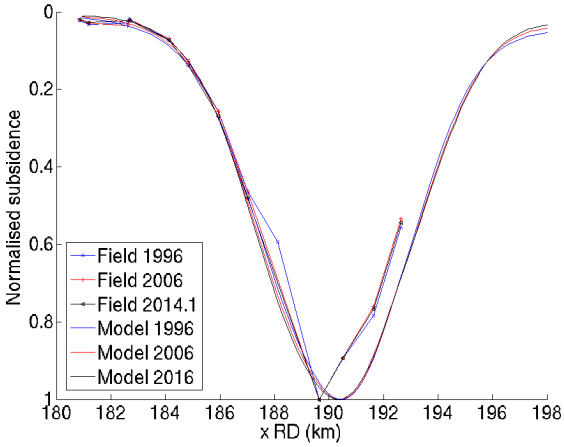

Figure 42. Comparison of subsidence bowl at three different times along E-W profile (Figure 36a) and leveling data (Figure 38). All have been normalized by maximum subsidence value.

7. Rocksalt flow- what about Groningen?

This section is motivated by the fact that there seems to be no mention of anomalous time dependent subsidence for the Groningen field, even though this is also salt-capped (see e.g. NAM, 2013). An additional model has been run, with a modified geometry more representative of Groningen, in order to investigate whether this apparent lack of anomalous behavior is consistent with the framework developed here for the Ameland field.

The geology of the two fields is very similar, the largest difference being their relative size. Mechanical properties that appear to have been used in the geomechanical analyses of Groningen subsidence are strikingly similar to the ones reported for Ameland (compare Mossop et al., 2011 to NAM, 2013). Second order differences in reservoir depth and layer thicknesses are neglected here to facilitate comparison of model results and to isolate the sensitivity of the reservoir lateral extent.

A Groningen-like axisymmetric simulation is attempted here. The gas reservoir radius

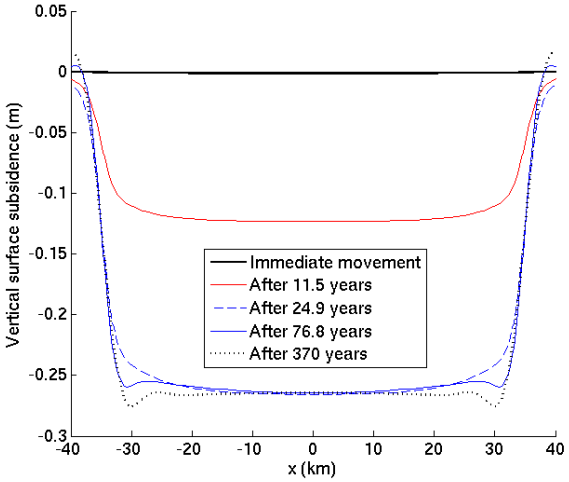

Figure 43. Illustrative subsidence bowl plotted at a number of different time instances. The case of the axisymmetric simulation of a Groningen-size reservoir that has the same layering and pressure history as the Ameland reservoir.

is set at 35 km. Material properties and vertical positions are set to be the same as for the axisymmetric Ameland models. Rocksalt flow is assumed to be linear with a viscosity of 10^{18} Pa.s as also used above for the Ameland field. The results for a linear pore pressure depletion at a rate of 2MPa/year for the first 25 years are shown in Figure 43. Subsidence bowls after 76.8 and 370 years show that the maximum subsidence is expected to be little affected by rocksalt flow. There is only a slight increase in its value. This is because shear stresses only occur at the edges of the compacting reservoir, which in the case of a Groningen-sized reservoir are remote from the point of maximum subsidence, and affect a far smaller percentage of the volume of the rocksalt around the compacting reservoir.

Noticeable changes in salt-induced subsidence only occur at the edges of the reservoir, but again their magnitudes are not as large as for Ameland, even thought rocksalt flow is active here too. They are also at locations where they are less likely to be detected by traditional geodetic techniques as they are possibly out of the main area of focus for subsidence monitoring. However they might be detectable through the processing of INSAR data. It should be noted that if significant anomalous time-dependent subsidence is actually observed over the middle of the Groningen field, this might be an indicator of the presence of another mechanism responsible for the time-dependence.

8. Discussion

We find major uncertainties in the time scale over which additional subsidence develops. The reason for this is that it depends on the rocksalt viscosity value and creep flow law, which is itself a function of a large number of factors (e.g. salt grain size, composition, impurities and water content, stress level) the majority of which are poorly constrained for the Ameland field. This means that the hypothesis that salt flow contributes to the observed time-dependence of subsidence cannot be rejected. On the contrary the hypothesis seems very plausible.

Rocksalt is a very complex material and a large number of flow laws are candidates for describing its creep behavior. This multitude of flow laws can lead to very different behavior at the ground surface. Identification of the correct type of flow law for the Zechstein rocksalt present in Ameland will require comparison of modeling results to field geodetic data, or sampling and direct experimental derivation of relevant parameters. The latter would require the laboratory tests to constrain creep behavior to be run at the very low strain rates relevant to the physical problem. As the Ameland salt is likely very similar to the Zechstein salt found at other locations in the North of the Netherlands it might be possible to constrain relevant aspects of salt behavior better by using data from other locations where time-dependent subsidence has also been observed, or using appropriate lab data on similar salt samples.

If rocksalt follows a linear flow law it might be possible to constrain the maximum value of the subsidence through simulations similar to the above. A combination of a power law creep and a linear flow law has the potential of causing subsidence in excess of that caused by linear salt flow. An investigation of the scatter in quoted values for the parameters in the power law flow equation has indicated that some combinations of input parameters yield excess maximum subsidence to the one calculated for the mean quoted values in the literatu-

re. The magnitude of this excess subsidence is measurable but nevertheless relatively small (less than 10% of the maximum subsidence value calculated for the mean rocksalt model input parameters).

An initial attempt at a comparison between model results and field data has highlighted the challenges posed by the large uncertainties in the geomechanical model inputs. For example magnitudes of subsidence can be matched by varying the compressibility of the reservoir material, a parameter that is spatially variable (see Mossop et al., 2011) and which is almost certainly stress-dependent, something that has been neglected here. Therefore the magnitudes of subsidence observed cannot be used as a meaningful hypothesis test at this stage of the life of the Ameland reservoir.

Data produced here for an axisymmetric representation of the Ameland field seem to indicate that a decrease in subsidence rates should have been observed in the field. Limited geodetic data analyzed as part of this study do not seem to show a decrease in subsidence as large as might be expected. It is possible that apart from the rocksalt flow mechanism there is another mechanism also active that can also enhance subsidence. An example of good candidates for this additional mechanism would be creep of the reservoir sandstone rock, or increased compressibility of the sandstone rock as it behaves inelastically at large effective stresses. These need to be investigated too.

Having access to horizontal surface displacements would be very useful for further testing of mechanisms for time-dependent subsidence with dynamic models.

Our full-3D results on an asymmetric reservoir indicate that movement of the deepest point of the subsidence point, if also observed in the field, might help verify what the best choice of rheological models is and whether rocksalt flow can cause significant time-dependent ground motions.

Overall, we present a framework that can help understand the effects of a number of factors on the additional rocksalt flow induced subsidence above a rocksalt-capped gas reservoir. As a number of such reservoirs exist in the Netherlands it might be possible to apply the knowledge gained here to other fields that have stopped producing, or to fields that show an anomalous time-dependence of subsidence. Readers are reminded however that rocksalt flow-induced subsidence seems to be a fraction of the total time-dependent subsidence.

9. Conclusions

Rocksalt flow potentially is a significant contributor to time-dependent subsidence in the Ameland field. Salt flow could enhance the subsidence predicted by elastic analyses by over 50%.

Time-dependent surface subsidence is driven first by shear stress-driven flow in the rocksalt layer resulting in rapid and significant subsidence beyond the elastic response.

A second, and slower phase is driven by pressure-driven flow and results in a decrease of the subsidence.

The thickness of the rocksalt layer and the vertical layering of the elastic properties significantly affect the maximum subsidence and the moment when this occurs.

The timescale over which the additional subsidence develops is subject to substantial uncertainty (few months to centuries).

The magnitude of the eventual subsidence also is poorly constrained.

The volume of the subsidence bowl is nearly completely controlled by the reservoir volume change, i.e., salt flow hardly affects subsidence bowl volume.

The majority of the uncertainties in the model predictions is caused by the wide range in possible material parameter values. Multiple flow laws have been proposed for rocksalt and result in different subsidence time scales and magnitudes. Better knowledge of the effective grain size of the rocksalt is important. Reservoir properties, in this study treated as elastic, influence the results significantly.

Our preliminary comparison to observations suggests that rocksalt flow cannot fully explain the surface subsidence. Further work would be required to firmly establish this conclusion.

10. Acknowledgements

The authors would like to acknowledge useful discussions with Anthony Mossop, Rob van Eijs and Hermann Baehr, all at Shell/NAM. We thank Roland Klees and Riccardo Riva from TU Delft for their help and flexibility that made it possible for TB to set aside his postdoc project for 4,5 months to work on the 3D model presented here.

11. Appendix A: GTECTON

11.1. Approach and assumptions

We use a finite element (FE) method to solve the mechanical equilibrium equations

$$\frac{\partial \sigma_{ij}}{\partial x_j} + \rho g_i = 0$$

where σ_{ij} is the ij-th element of the Cauchy stress tensor, ρ is density, and g_i is the component of the gravity acceleration in the i-th coordinate direction. We solve for displacements in a Lagrangian framework. We use the Utrecht University GTECTON software platform to iteratively solve the matrix equations (Govers and Wortel, 1993; Govers and Wortel, 1999; Govers and Wortel, 2005). Constitutive equations are based on compressible, isotropic elasticity (defined by Young's modulus E and Poisson's ratio ν) and by incompressible viscous flow. The total strain rate is the sum of the elastic and viscous strain rate. Assuming axisymmetry, the resulting equations between components of the strain rate ($\dot{\varepsilon}_{ij}$) and stress tensor

$$\begin{aligned}
\dot{\varepsilon}_{rr} &= \frac{1}{E}\left[\dot{\sigma}_{rr} - \nu(\dot{\sigma}_{zz} + \dot{\sigma}_{\theta\theta})\right] + \frac{(\sigma_E/\eta)^{n-1}}{6\eta}\left[2\sigma_{rr} - \sigma_{zz} - \sigma_{\theta\theta}\right] \\
\dot{\varepsilon}_{zz} &= \frac{1}{E}\left[\dot{\sigma}_{zz} - \nu(\dot{\sigma}_{rr} + \dot{\sigma}_{\theta\theta})\right] + \frac{(\sigma_E/\eta)^{n-1}}{6\eta}\left[2\sigma_{zz} - \sigma_{rr} - \sigma_{\theta\theta}\right] \\
\dot{\varepsilon}_{\theta\theta} &= \frac{1}{E}\left[\dot{\sigma}_{\theta\theta} - \nu(\dot{\sigma}_{rr} + \dot{\sigma}_{zz})\right] + \frac{(\sigma_E/\eta)^{n-1}}{6\eta}\left[2\sigma_{\theta\theta} - \sigma_{rr} - \sigma_{zz}\right] \\
\dot{\varepsilon}_{rz} &= \frac{1+\nu}{E}\dot{\sigma}_{rz} + \frac{(\sigma_E/\eta)^{n-1}}{2\eta}\sigma_{rz}
\end{aligned} \tag{A.1}$$

where r, z, and θ refer to the radial, axial and tangential directions, a dot refers to the time derivative, and σ_E is the maximum deviatoric shear stress defined by

$$\sigma_E = \sqrt{\frac{\sigma_{rr}^2 + \sigma_{zz}^2 + \sigma_{\theta\theta}^2 - \sigma_{rr}\sigma_{zz} - \sigma_{rr}\sigma_{\theta\theta} - \sigma_{zz}\sigma_{\theta\theta}}{3} + \sigma_{rz}^2} \tag{A.2}$$

We assume that viscosities are isotropic. In accordance with rock mechanical experiments, we assume that the bulk viscosity is infinite so that η represents the shear viscosity. The stress power n can be used to model so-called non-linear (power-law) viscous flow. Equivalent equations for two- and three-dimensional geometries can be found in Govers and Wortel (1993) and Govers and Wortel (2005), respectively.

Non-linearity arising from geometry change is accounted for using a residual force update technique (McMeeking and Rice, 1975; Govers and Wortel, 1999).

Note that as the mechanical equilibrium equations are linear and superposition of solutions applies, the stress quantities solved for are stress perturbations on top of the initial stresses that are in equilibrium with gravity forces (as initial stresses will not affect production-induced displacements). In addition, for the porous reservoir rock material, the stresses in equation (A.1) which are solved for are effective stresses, i.e. total stresses minus the reservoir

pore-fluid pressure. Essentially this is equivalent to assuming a Biot coefficient of 1 for the reservoir material, and assuming that the entirety of the production-induced pore pressure decrease results in a stress increase felt by the solid skeleton of the reservoir rock material.

11.2. Benchmarking

The GTECTON codes were previously benchmarked for a wide range of elastic and visco-elastic problems. It has been used as the main platform for research papers by the Utrecht University Tectonophysics group. As part of the present project, we validated the numerical codes against an analytical solution for the elastic deformation around a circular cavity in an elastic half-space (Verruijt, 1996; 1998), where a uniform pressure acts on the interior wall of the cylinder.

12. References

Breunese, J.N., van Eijs, R.M.H.E, de Meer, S. and Kroon, I.C. (2003) Observation and prediction of the relation between salt creep and land subsidence in solution mining – The Barradeel case, Proceedings, SMRI Conference, Chester.

Carter, N.L., Horseman, S.T., Russel, J.E. and Handin, J. (1993) Rheology of rocksalt. Journal of Structural Geology 15, pp. 1257-1271.

Crouch, S.V., Baumgartner, W.E.L., Houlleberghs, E.J.M.J. and Walzebuck, J.P. (1996) Development of a tight gas reservoir by a multiple fracced horizontal well: Ameland-204, the Netherlands. In Rondeel et al. (eds) Geology of gas and oil under the Netherlands, Kluwer Academic, The Netherlands, pp. 93-102.

Geertsma, J. (1973), Land subsidence above compacting oil and gas reservoirs, J. Petrol. Tech., 25, 734-744.

Govers, R. and Wortel, M.J.R. (1993) Initiation of asymmetric extension in continental lithosphere. Tectonophysics, 223, pp. 75-96.

Govers, R. and Wortel, M.J.R. (1999) Some remarks on the relation between vertical motions of the lithosphere during extension and the "necking depth" parameter inferred from kinematic modeling studies. Journal of Geophysical Research, 104(B10), pp. 23245-23254.

Govers, R. and Wortel, M.J.R. (2005) Lithosphere tearing the STEP faults: response to edges of subduction zones. Earth and Planetary Science Letters, 236, pp. 505-523.

Houtenbos, A.P.E.M. (2011), Bodemdaling Waddenzee 1977-2011.

Marketos G., Govers R.M.A. and Spiers C.J. Ground motions induced by a producing hydrocarbon reservoir that is overlain by a viscoelastic rocksalt layer: A numerical model. In revision for Geophysical Journal International, June 2015.

Marquenie, J.M. and Doornhof, D. (2005). Bodemdaling en gaswinning. Retrieved from Waddenzee.nl on April 14th, 2015.

McMeeking, R.M. Rice, J.R., Finite element formulations for problems of large elastic-plastic deformation, International Journal of Solids and Structures 11(1975) 601-616.

Mossop, A., van der Wal, O. and van Eijs, R. (2011) Subsurface technical report: Subsidence modelling of Ameland Fields, NAM Report, Assen.

NAM (2013) Technical addendum to the winningsplan Groningen 2013: Subsidence, induced earthquakes and seismic hazard analysis in the Groningen Field.

Orlic, B. and Wassing, B.B.T. (2013) A study of stress change and fault slip in producing gas reservoirs overlain by elastic and viscoelastic caprocks. Rock Mech. Rock. Eng. 46 pp. 421-435, doi: 10.1007/s00603-012-0347-6.

Prij, J. (1991). On the design of a radioactive waste repository. PhD. thesis, Univ. of Twente. ISBN 90-375-0261-X. pp 227.

Spiers, C.J. and Carter, N.L. (1998) Microphysics of rocksalt flow in nature. In: Aubertin M. and Hardy H.R. (eds.), Proceedings of the 4th Conference on the Mechanical Behavior of Salt, Trans Tech Publication Series on Rock and Soil Mechanics 22, pp. 115-128.

Spiers, C.J., Schutjens, P.M.T.M., Brzesowsky, R.H., Peach, C.J., Liezenberg, J.L. and Zwart, H.J. (1990) Experimental determination of constitutive

parameters governing creep of rocksalt by pressure solution. In: Knipe, R.J., Rutter, E.H. (Eds.), Deformation Mechanisms, Rheology and Tectonics Geological Society of London Special Publication, 54, pp. 215–227.

Ter Heege, J.H., De Bresser, J.H.P. and Spiers, C.J. (2005) Rheological behaviour of synthetic rocksalt: the interplay between water, dynamic recrystallization and deformation mechanisms. Journal of Structural Geology 27, pp. 948–963.

Urai, J.L. and Spiers, C.J. (2007) The effect of grain boundary water on deformation mechanisms and rheology of rock salt during long-term deformation. In: Wallner M., Lux K.H., Minkley W. and Hardy H.R. (eds.), Proceedings of the 6th Conference on the Mechanical Behavior of Salt - Understanding of THMC Processes in Salt, Taylor and Francis.

van Keken, P.E., Spiers, C.J., van den Berg, A.P., and Muyzert, E.J. (1993) The effective viscosity of rocksalt: implementation of steady state creep laws in numerical models of salt diapirism. Tectonophysics, 225, pp. 457–476.

Verruijt A. (1996) Complex variable solutions for tunnelling problems. Report, Geotechnical Laboratory, Delft University of Technology.

Verruijt, A. (1998), Deformations of an elastic half plane with a circular cavity, Int. J. Solids Struct., 35(21), 2795–2804, doi: 10.1016/S0020- 7683(97) 00194-7.

Warners-Ruckstuhl, K.N., Govers, R., Wortel, R., 2013. Tethyan collision forces and the stress field of the Eurasian Plate. Geophys. J. Int. 195, 1–15. doi:10.1093/gji/ggt219.